# Fracture universality in amorphous nanowires

Kun Zhao [a,b], Yun-Jiang Wang [a,b,*], Penghui Cao [c,*]

[a] *State Key Laboratory of Nonlinear Mechanics, Institute of Mechanics, Chinese Academy of Sciences, Beijing 100190, China*
[b] *School of Engineering Science, University of Chinese Academy of Sciences, Beijing 100049, China*
[c] *Department of Mechanical and Aerospace Engineering, University of California, Irvine, CA, 92697, USA*

## ARTICLE INFO

## ABSTRACT

Crystalline nanowires exhibiting a wide range of size-dependent fracture and failure modes have been extensively studied, yet the fracture behaviors of amorphous materials and their size dependence remain elusive. Here extensive atomistic simulations are performed to reveal the deformation and fracture behaviors in a broad class of amorphous nanowires with varying sizes, including CuZr, CuZrAl, FeP, Si, and a ductile Lennard-Jones system. It is found that the fracture strain $\varepsilon_f$ increases with nanowire length $L$ but decreases with diameter $D$, which exhibits a linear relationship with the diameter-to-length ratio as $\varepsilon_f \propto D/L$, —a scaling law valid in these five distinct glassy systems understudied. We develop a theoretical model, capturing the size of plastic zone at plastic yielding and its vital role in governing the final fracture strain, which shows an agreement with the simulation data. By taking into account the intrinsic atomic-level ideal strain, remarkably, all the size-dependent fracture strain data collapse, signifying the universality of fracture nature in a broad range of glassy materials.

## 1. Introduction

Fracture of materials is a representative of multi-scale phenomena down to atomic scale, which has attracted massive attention in materials science and mechanics. However, the microscopic fracture mechanics of materials remains elusive and keeps on puzzling the community for decades especially when the failure mechanism is novel and in contrast with the traditional fracture mechanisms such as brittle crack propagation involving critical role of new free surface creation as explained in the Griffith theory of fracture (Griffith, 1921). Relevant study of fracture ranges from macro-scale, in which plastic deformation mainly occurs in an unstable and local region that accelerates the crack propagation, to the nanometer scale which assumes microscope defect and atomic displacement field promote irreversible deformation (Taloni et al., 2018). The common sense in a series of crystalline (Lu et al., 2009; Wu et al., 2012; Tao et al., 2018) and amorphous materials (Kumar et al., 2011; Şopu et al., 2016; Qu et al., 2019) generally is that larger samples are more sensitive to fracture. The size effect of fracture is hard to describe through continuum mechanics framework: the stress is constant regardless of the sample length if the cross section is the same. From theoretical point of view, some endeavors with critical role of stress components were pursued to explain the size effect on materials' failure (Christensen et al., 2018). And sometimes extreme value theory was also adopted to clarify the mechanism underlying fracture statistics (Taloni et al., 2018). However, almost all the theoretical analyses more or less exist limitations, failing to fully forecast the size effect in fracture of materials.

The fracture issue becomes even more intractable once it encounters new deformation mechanisms in unconventional materials. Since first reported by Klement et al. (1960) in 1960s, the disordered material metallic glasses (MGs) have received extensive

attention due to their unique mechanical properties such as strong, high elastic limit, and superior toughness (Ashby and Greer, 2006). Such kind of amorphous solids fracture via a novel cavitation mechanism in front of crack, as initially predicted by atomistic simulations (Murali et al., 2011; Guan et al., 2013) and recently confirmed by experimental observation (Shen et al., 2021; Pan et al., 2015). The plastic deformation mechanism of amorphous solids is also different from the dislocation accommodated plasticity in crystals, in the former case the elementary deformation unit is the so-called shear transformation (Argon, 1979; Falk and Langer, 1998), or the Johari–Goldstein $\beta$ relaxation of nanoscale which contains a few tens of atoms (Yu et al., 2012, 2013; Yang et al., 2021a). Such unusual deformation and fracture mechanisms challenge the conventional Griffith's scenario and cast difficulty in rationalization of the mechanical properties, e.g., the size-dependent fracture of amorphous materials.

Fracture resistance is an essential precondition for the application of MGs as potential structural materials (Sun and Wang, 2015). The bottleneck of amorphous solids is the catastrophic failure via shear banding owing to the lack of strain hardening mechanisms (Pan et al., 2020; Lewandowski et al., 2005; Greer and Ma, 2007; Yang et al., 2021b; Cao et al., 2018). Recently, it has become realized that the plasticity of MG can be enhanced by reducing sample size (Guo et al., 2007; Jang and Greer, 2010; Kumar et al., 2011; Luo et al., 2016; Yang et al., 2021a). There have been extensive experiments exhibiting elevated toughness (Gludovatz et al., 2014), improved strength (Greer and De Hosson, 2011; Wang et al., 2012; Li et al., 2017), extensive elasticity (Tian et al., 2012) and ductile necking instead of shear banding mechanism have been seen in nanoscale MGs (Greer and De Hosson, 2011; Chen et al., 2013; Tian et al., 2013; Gu et al., 2014). All of the observations are indicative of the size effect on mechanical properties of MGs, which may provide a strategy to avoid catastrophic failure. On the other hand, atomistic simulations also confirm that nanoscale amorphous materials tend to be more ductile than their bulk counterparts (Wei et al., 2010; Zhou et al., 2015; Şopu et al., 2016; Zhang et al., 2021). A transition in MG failure mode with change in aspect ratio is observed (Sha et al., 2014). Simple model was able to predict a critical size for the ductile-to-brittle transition in MG nanowires (Şopu et al., 2016). All studies confirm the existence of size effect and point to the "smaller is stronger" trend in MGs (Jang and Greer, 2010; Greer and De Hosson, 2011; Sha et al., 2017). Importantly, ductility is simultaneously enhanced by size reduction which is on the contrary to some of their crystalline counterparts (Tian et al., 2012).

A universal relationship between extrinsic size effect and fracture of crystalline nanowire has been clarified (Wu et al., 2012). Albeit some phenomena are observed, the size effect in fracture of amorphous solids is still disputable. It is mainly because of the less understood shear localization mechanism, especially at atomic and micro-scales (Wang et al., 2022; Cao et al., 2019). And sometimes different localization mechanisms compete to dominate fracture according to different laws (Wu et al., 2009; Zhou et al., 2015). Competing size effect also matters, e.g., it is nontrivial to reveal the respective roles of diameter and length of wire in fracture (Şopu et al., 2016). The missing information is how the structural disorder interacts with the basic deformation unit and helps the isolated local deformation evolve into shear localization that leads to fracture in amorphous materials (Taloni et al., 2018). During the dynamic localization process, how the extrinsic geometries of MG samples come into play is still unclear.

To settle the issues, extensive molecular dynamics (MD) simulations are performed to investigate the role of size in fracture of amorphous nanowires, taking a variety of amorphous systems with different combinations of diameter, length, and interatomic interactions as representatives. Scaling relationship between fracture strain and system dimensions are carefully analyzed and further interpreted by a developed mechanistic models. Considering the intrinsic atomistic ideal strain, a universal size-dependent fracture law is established, highlighting the commonality of fracture origin down to bonding nature of amorphous materials.

## 2. Atomistic simulations and deformation models

MD simulations using the software LAMMPS (Plimpton, 1995) are performed to elucidate the size effect in fracture of MG nanowires. While a binary $Cu_{50}Zr_{50}$ MG (interacted with Finnis–Sinclair type embedded method potential proposed by Mendelev et al., 2009) is simulated as a prototypical amorphous materials, other systems with different bonding nature are also considered to generalize the observations, which include Si (Stillinger–Weber potential) (Stillinger and Weber, 1985), $Cu_{64}Zr_{36}$ (Mendelev et al., 2009), $Zr_{46}Cu_{46}Al_8$ (Cheng et al., 2009), $Fe_{80}P_{20}$ (Ackland et al., 2004), as well as the general Lennard-Jones (L-J) model (Kob and Andersen, 1995).

To simulate fracture of amorphous nanowires, a cubic $Cu_{50}Zr_{50}$ MG sample with dimensions of $L_x, L_y, L_z$ = 7, 7, 7 nm, containing 19652 atoms, is created by cooling from liquid. Using periodic boundary condition in all three directions, the equilibrium temperature and external pressure are set as 2000 K and 0 GPa, respectively. After equilibrating the glass-forming liquid for 2 ns at 2000 K under $NPT$ ensemble (constant number of atoms, constant pressure and constant temperature), we decrease temperature to 0.1 K with a cooling rate of $10^{10}$ K/s. The sample is then thoroughly relaxed at 0 K. To control the temperature and pressure in isothermal–isobaric ensemble, Nosé–Hoover thermostat Nosé (1984), Hoover (1985), and Parrinello–Rahman barostat Parrinello and Rahman (1981) are used. The MD time step is 2 fs.

In order to generate a series of MG nanowires with different size, the initial sample is duplicated five times in both $x$ and $y$ directions, 35 times in the $z$ direction (uniaxial tensile direction). Via this operation a huge bulk sample containing 22 108 500 atoms with dimensions of $L_x, L_y, L_z = 35, 35, 315$ nm is prepared. The large sample is allowed to relax for 1 ns to ensure an energetically favored configuration. Next, cylindrical-shaped nanowires are produced by cutting the bulk sample. For the nanowires, periodic boundary condition is imposed along the tensile direction and the lateral directions are of free boundary condition.

Before loading, the nanowires are first heated up to 10 K and equilibrated for 1 ns under the $NPT$ ensemble to relax the surface and residual stress. Then, uniaxial tensile deformation with a constant strain rate of $4 \times 10^8$ s$^{-1}$ is applied at 10 K under the $NVT$ (constant number of atoms, constant volume and constant temperature) ensemble, until to a global strain at which fracture happens. In total, 45 $Cu_{50}Zr_{50}$ nanowires with different length (20 to 150 nm) and diameter (5 to 30 nm) combinations are prepared for the

fracture tests. The same strategy is performed on other five types of MG nanowires. The current modeling and simulation focusing on cryogenic temperature (10 K) aim to rule out thermal effects and isolate the size effects on pure stress-driven deformation of various glass systems. We note that the glassy systems under consideration (CuZr, CuZrAl, FeP, Si) could have different thermal sensitivities. At the 10 K (close to molecular statics), we are able to connect the system-level fracture strain to the intrinsic atomic-level ideal strain. When the temperature increases to room temperature or higher, the thermally activated processes, such as atomic diffusion, will participate in the deformation, favoring necking-like flow. It is reasonable to speculate that, at room and elevated temperatures, the diffusion could increase fracture strain and ductility and shift the fracture mode from the shear band towards necking.

The atomistic configurations are visualized by OVITO software (Stukowski, 2010). The atomic-scale deformation mechanism of samples are characterized by the non-affine squared displacement (Falk and Langer, 1998) and the local atomic shear strain invariant (von Mises strain $\eta_{\text{Mises}}$) (Shimizu et al., 2007), as both have been implemented in OVITO. The non-affine squared displacement is a unique structural metric describing information about nonelastic deformation in disordered materials, which reads

$$D_{\min}^2(t, \Delta t) = \sum_n \sum_i \left\{ \mathbf{r}_n^i(t) - \mathbf{r}_0^i(t) - \sum_j \left( \delta_{ij} + \varepsilon_{ij} \right) \times \left[ \mathbf{r}_n^j(t - \Delta t) - \mathbf{r}_0^j(t - \Delta t) \right] \right\}^2, \tag{1}$$

where $\mathbf{r}_n^i(t)$ is the position of the $i$th atom at time $t$ considering $n$ neighbors within a reasonable cutoff distance. The minimization of $D_{\min}^2$ yields a best mapping deformation gradient tensor with component $\varepsilon_{ij}$ from the reference configuration to the current one. Further, the local von Mises strain invariant is defined via $\varepsilon_{ij}$ as (Shimizu et al., 2007)

$$\eta_{\text{Mises}} = \sqrt{\eta_{XY}^2 + \eta_{XZ}^2 + \eta_{YZ}^2 + \frac{\left( \eta_{XX} - \eta_{YY} \right)^2 + \left( \eta_{XX} - \eta_{ZZ} \right)^2 + \left( \eta_{YY}^2 - \eta_{ZZ}^2 \right)^2}{6}}, \tag{2}$$

in which $\eta_{\alpha\beta}$ are the components of the strain gradient tensor of atom $i$. It has been shown widely in the literature as a fairly nice metric to level local nonelastic deformation in disordered medium.

## 3. Simulation results

### 3.1. Size-dependent fracture

The atomistic simulations inform clearly that fracture in MG nanowires are size dependent. Fig. 1a shows the stress–strain curves of the 11 considered $Cu_{50}Zr_{50}$ nanowires with constant diameter ($D = 20$ nm) but varying length $L$ (20 to 140 nm). Regardless of
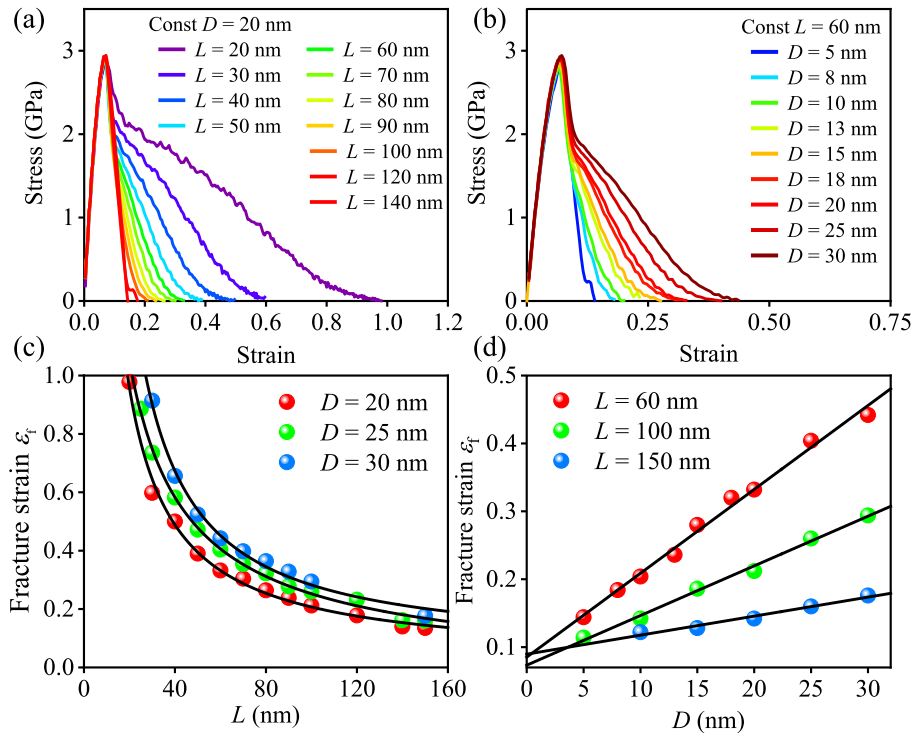


**Fig. 1.** Size-dependent fracture of $Cu_{50}Zr_{50}$ metallic glass nanowires. Uniaxial tensile stress–strain curves of the nanowires with (a) constant diameter 20 nm and varying length from 20 to 140 nm, and (b) constant length 60 nm but varying diameter from 5 to 30 nm. (c) Fracture strain decreases with increasing length while the diameter is fixed. The solid curves represent best nonlinear fit according to $\varepsilon_f \propto 1/L$. (d) A linear relationship exists between the fracture strain and diameter of the nanowires while the length is fixed.
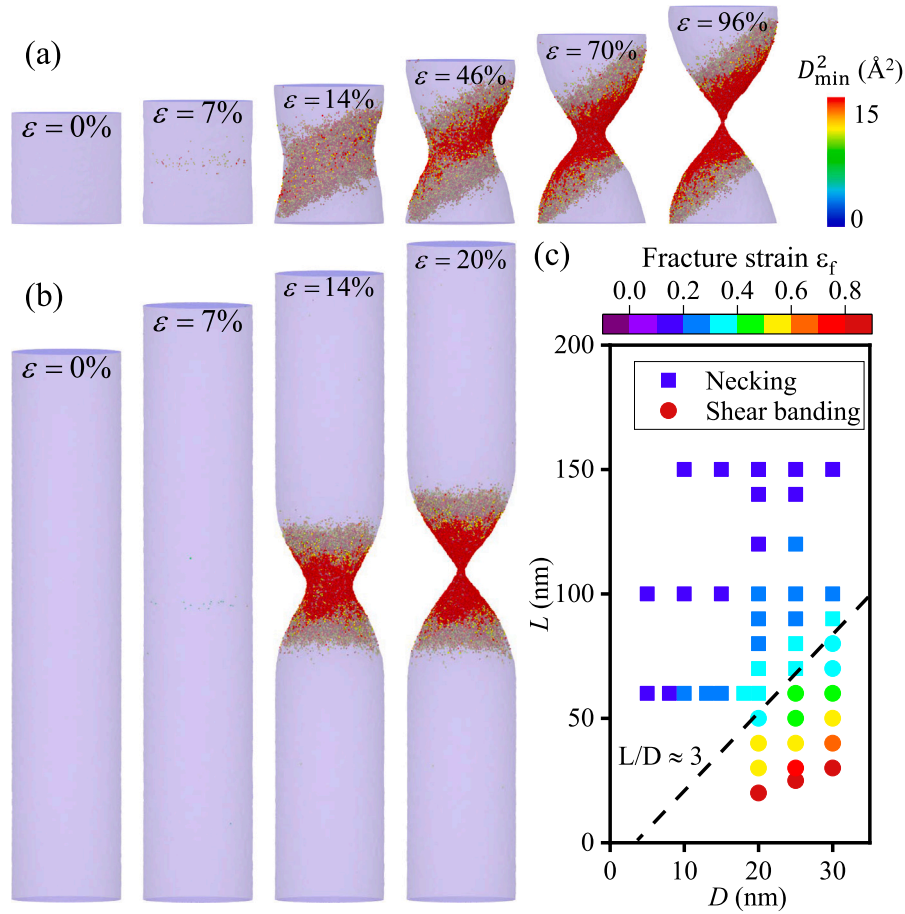
**Fig. 2.** Size-dependent fracture diagram. (a) Shear banding in fat wire with $L = 20$ nm, and $D = 20$ nm. (b) Necking in thin wire with $L = 100$ nm, $D = 20$ nm. Atoms are colored by the atomic-scale non-affine squared displacement. Only atoms with displacement more than 10 Å are shown for clarity. (c) Fracture mechanism map of the MG nanowires informed by the magnitude of fracture strain $\varepsilon_f$. Squares indicate failure by necking, and circulares failure by shear banding. The color of symbols denotes magnitude of fracture strain. A border $L/D \approx 3$ well separates the two regimes dominated by distinct fracture modes.

nanowire length, stresses of all nanowires increase linearly at the beginning of strain until to a yield strain $\varepsilon_y$ ($\approx 0.07$). For the plastic deformation, the nanowires show entirely different mechanical behaviors. The wire with length $L = 20$ nm fails after many serrations in the stress–strain curve, suggesting the existence of successive local plastic events that promote ductility. However, the long nanowire with length $L = 140$ nm fails catastrophically in a brittle manner. The ductility, or strain at failure, obviously decreases with increasing wire length. In addition, ductility is improved with increasing wire diameter, while length is kept constant as $L = 60$ nm, as shown in Fig. 1b. The diameter effect on fracture may be attributed to a change in the fraction of surface atoms which is more active in plastic deformation (Wei et al., 2010; Swallen et al., 2007). To quantify the observation, we define a fracture strain $\varepsilon_f$ at which stress has decayed to zero. Fig. 1c–d show the relationship between $\varepsilon_f$ and wire length $L$ and diameter $D$, respectively. For a first order approximation, $\varepsilon_f \propto 1/L$ and $\propto D$. These findings confirm a strong size effect on fracture of MG nanowires. On the basis of these data, we preliminarily assume that $\varepsilon_f$ scales proportionally to $D/L$, i.e., the reciprocal of aspect ratio. We will provide argument for this scaling law in the rest of this work.

### 3.2. Size-dependent fracture diagram

Note only the fracture strain, but also the fracture mode is dimension specific. To further explore the atomic-scale mechanism of fracture, we display a sequence of MD snapshots of samples visualized by the magnitude of the non-affine squared displacement (Falk and Langer, 1998) during deformation in Fig. 2a–b. We select two nanowires deliberately with the same diameter of 20 nm, but different length of 20 nm and 100 nm, respectively. Regardless of the length or aspect ratio, both wires are uniformly elongated, up to a tensile strain as high as 0.07. Once the applied strain exceeds yield strain, both two nanowires show radically different deformation behaviors although strain localization occurs in both cases. Plastic deformation in the fat wire mainly occurs in a narrow shear band region, whereas the thin wire undergoes necking phenomenon. Furthermore, the necking region in the thin wire shrinks rapidly even tensile strain increases moderately. Instead, once shear band sets in the fat wire with smaller aspect ratio
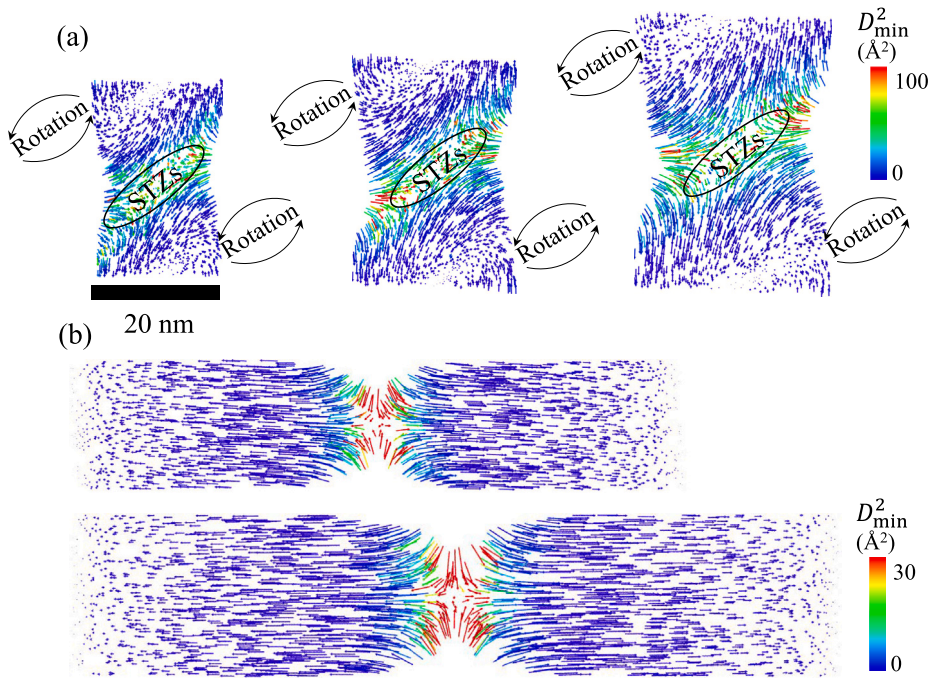
**Fig. 3.** The displacement field in $Cu_{50}Zr_{50}$ metallic glass nanowires with (a) small aspect ratio 1:1 and (b) large aspect ratio 4:1. (a) From left to right $D = 20$, $D = 25$, $D = 30$ nm under tensile strain $\varepsilon = 0.4$. There are two rotations in top-left corner and bottom-right corner, respectively. Many small STZs exist between the two rotation regions. Shear band formed due to the interaction of rotations and STZs. (b) From up to down $D = 20$ and $D = 25$ nm at $\varepsilon = 0.1$. Atoms in the necking region move from surface into inner core region. For clarity, the displacement vector has been scaled by 0.5.

(1:1), the following slip is more or less arrested and it bears more plastic strain in the same region. This has been reflected in the stress–strain curves in Fig. 1. It is not intuitive up to now that a fat wire experiences shear banding, however, it exhibits enhanced ductility compared with a thin wire failed by necking. Similar phenomenon about size effect in deformation of nanoscale MGs has been observed by atomistic simulations previously (Şopu et al., 2016; Wei et al., 2010). All calculated fracture strains $\varepsilon_{\mathrm{f}}$ of $Cu_{50}Zr_{50}$ samples with different geometries are summarized in Fig. 2c, which enables to build a fracture diagram of the nanowires as functions of their length and diameter. A boundary about $L/D = 3$ clearly separates the two fracture modes, i.e., shear banding in fat wires and necking in thin ones. The results suggest that aspect ratio plays a dominant role in fracture of MG nanowires.

### 3.3. Atomic-scale mechanism underlying shear banding and necking

The size-dependent fracture can be traced to the source of atomic-scale deformation pattern. More details about the localization process are further illustrated in Fig. 3, by showing the displacement field of several nanowires with aspect ratio 1:1 and 4:1, respectively. In Fig. 3a, we show three nanowires with the same aspect ratio 1:1 but different size (varying $D$ and $L$ accordingly). Although the size is different, they show identical displacement pattern, therefore, only aspect ratio matters. The lengths of nanowires from left to right are 20, 25, 30 nm, respectively. Each nanowire shows pronounced plastic deformation at strain magnitude of 0.4. For the sake of clarity, only a slice of 1 nm is plotted here perpendicular to the paper direction. The displacement vectors are painted in colors according to their atomic non-affine squared displacement ($D_{\mathrm{min}}^2$). It is seen that two rotation regions appear at the top-left and the bottom-right parts of the wire and collective atomic rearrangements called shear transformation zones (STZs) (Argon, 1979) exist in between. It is generally known that STZs are fundamental plasticity carriers and triggering factors of shear band in the general amorphous materials (Argon, 1979). Thus, highly localized shear band forms by percolation of STZs with the help of neighboring rotations, as explained by Şopu et al. in the literature (Şopu et al., 2017). These fat nanowires deform and finally fail via shear banding mode. On the other hand, there are two thin wires with the same aspect ratio 4:1, the deformation is illustrated at strain 0.1, as shown in Fig. 3b. The lengths of the two nanowires are 80 and 100 nm, respectively. Rather than shear banding, clear necking deformation is observed. Plastic atoms have populated in a narrow but uniform region in the middle of the wires. Flow of the active atoms occurs from surface to the inner core of wire, which leads to the necking phenomenon and the final fracture by necking at larger strain. These atomic-scale analyses provide compelling evidences for the fact that nanowires with different aspect ratio present distinct localization process, resulting in two fracture modes.
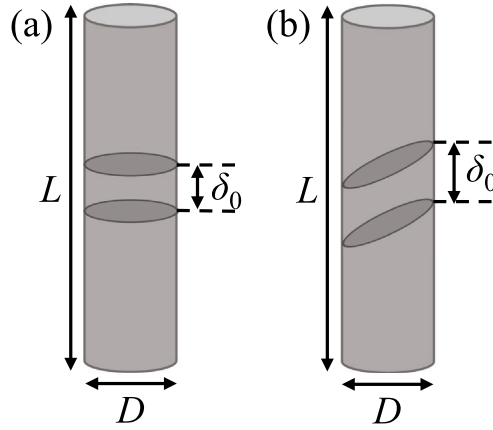
**Fig. 4.** Schematic illustration of the localized deformation in a narrow region of length $\delta_0$ at $\varepsilon = 0$ for (a) necking mode and (b) shear banding mode. A scaling factor $L/\delta_0$ translates the fracture strain into a physically effective strain.
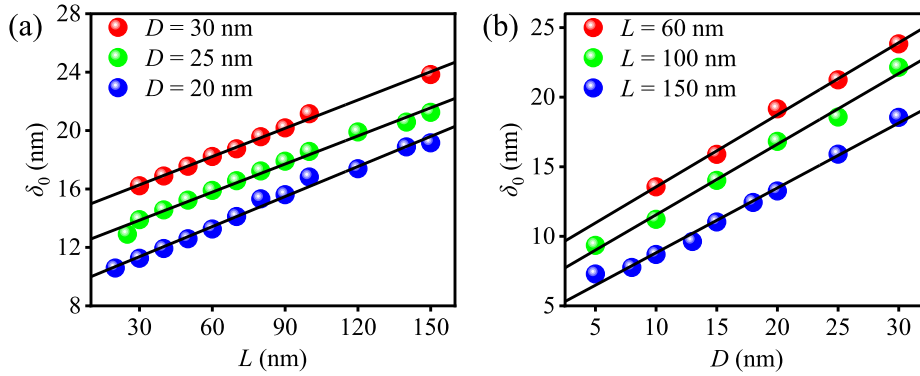


**Fig. 5.** The dependence of inherent localization length $\delta_0$ on (a) the length $L$ and (b) diameter $D$ of the $Cu_{50}Zr_{50}$ metallic glass nanowires.

## 4. Mechanistic fracture models

### 4.1. Inherent localization length

With the simulation data, it is possible to build a quantitative relationship between fracture and geometry, which is enabled by continuum models. In order to quantify the correlation among wire geometries, fracture strain $\varepsilon_f$ and fracture modes, we develop two mechanistic models corresponding to shear banding and necking, respectively. According to the deformation patterns demonstrated in Fig. 2, we assume that all plastic deformation occurs in a narrow region with an inherent length $\delta_0$ (at the beginning of deformation), as shown schematically in Fig. 4. Here we assume $\delta_0$ is size-dependent and can be measured by examining the spatial distribution of atomic shear strain Yang and Dai (2021). To be more specific, there is a visual peak in the spatial distribution of the averaged atomic shear strain at the specific strain state when localized region has already been formed. The width of the peak is the length of the localized region at this moment, which is used to derive $\delta_0$ at the beginning of macroscopic strain. The measurement of $\delta_0$ is entirely from atomic shear strain and is reasonable. For further details of the derivation of inherent localization length, the readers are referred to Appendix. An explicit correlation between the localization length $\delta_0$ and the size of nanowires is reported in Fig. 5. The trend is that $\delta_0$ is proportional to both length and diameter of nanowires, obeying a well-defined linear relationship. It is worth noting that, for different diameters, the slope of $\delta_0$ versus length remains approximately the same, and vice versa. Consequently, there is no coupling between the effect of length on $\delta_0$ and that of diameter on $\delta_0$. They obeys independent rules and can be expressed mathematically

$$\delta_0 = aL + bD, \tag{3}$$

where $a$ and $b$ are constant that be can evaluated by the slopes of lines in Fig. 5.
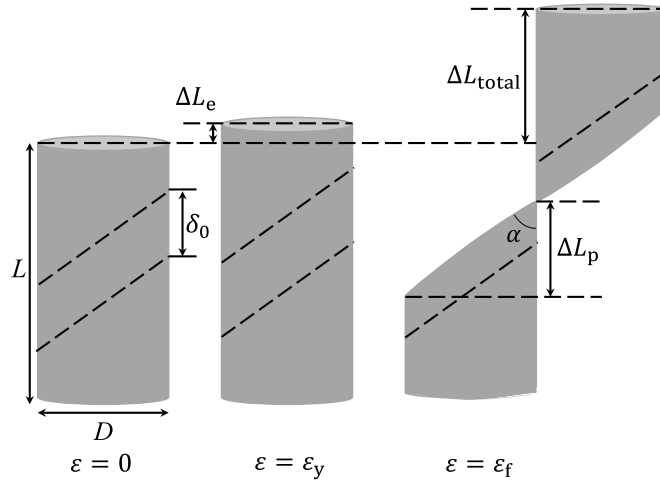
**Fig. 6.** Schematic illustration of fracture via shear banding. Nanowire has a cylindrical cross section. Only a nanowire with low aspect ratio deforms in shear banding mode under uniaxial tension.

## 4.2. Effective strain

With the knowledge established we are enable to define a physically relevant effective strain by geometrical transformation. For the $Cu_{50}Zr_{50}$ nanowires tested here, the dimensionless parameters existing in Eq. (3) is determined as $a \approx 0.046$, and $b \approx 0.483$ from Fig. 5. It is evident that $\delta_0$ is more sensitive to $D$ than $L$, considering that $D$ determines the ratio of the surface atoms to volume ones. And the atoms in the outer rim are of much more mobility than the others and, thus, $D$ affects more on the localization behaviors, as also explained by Bonfanti et al. (2018).

Now it is ready to translate the nominal fracture strain to a physically relevant effective strain $\varepsilon_{eff}$ via an amplification factor $L/\delta_0$, i.e.,

$$\varepsilon_{eff} = \frac{\left(\varepsilon_f - \varepsilon_y\right) L}{\delta_0} + \varepsilon_y. \tag{4}$$

Note that although the localized region of shear banding mode is of some angle to the tensile direction, the transformation from the nominal fracture strain to a physically relevant effective strain is also rational. Compared with the fracture strain $\varepsilon_f$, the effective strain $\varepsilon_{eff}$ has excluded the extrinsic localization factor such that it reflects the intrinsic deformation of wires and facilitates explaining localization mechanisms in fracture.

## 4.3. Shear banding model

In the following we build two simple but powerful theoretical models for predicting fracture of nanowires based on shear banding and necking, respectively. For different deformation modes, the total translational displacement along the axial direction $\Delta L_{total}$ is composed of two parts, i.e., the elastic displacement $\Delta L_e$ and the plastic displacement $\Delta L_p$, respectively. The wires exhibit uniform elongation during the elastic stage. Thus, we mainly focus on the plastic displacement to understand deformation localization. For the shear banding mode sketched in Fig. 6, the plastic deformation occurs in a dominate slip region. We observe from MD snapshots that the slip direction has an angle $\alpha \approx 51°$ with respect to the wire axis (i.e., the uniaxial loading direction). Then the plastic deformation (in terms of plastic elongation) can be expressed in two ways, i.e.,

$$\Delta L_p = \delta_0 \left(\varepsilon_{eff} - \varepsilon_y\right) = \frac{D}{\tan \alpha}. \tag{5}$$

Solving above equation, one obtains the magnitude of effective strain $\varepsilon_{eff}$ as

$$\varepsilon_{eff} = \frac{D}{\delta_0 \tan \alpha} + \varepsilon_y. \tag{6}$$

Combining Eqs. (3), (4) and (6), one is able to postulate that how the fracture strain $\varepsilon_f$ in shear band depends on the aspect ratio in terms of

$$\varepsilon_f = \frac{D}{L \tan \alpha} + \varepsilon_y. \tag{7}$$
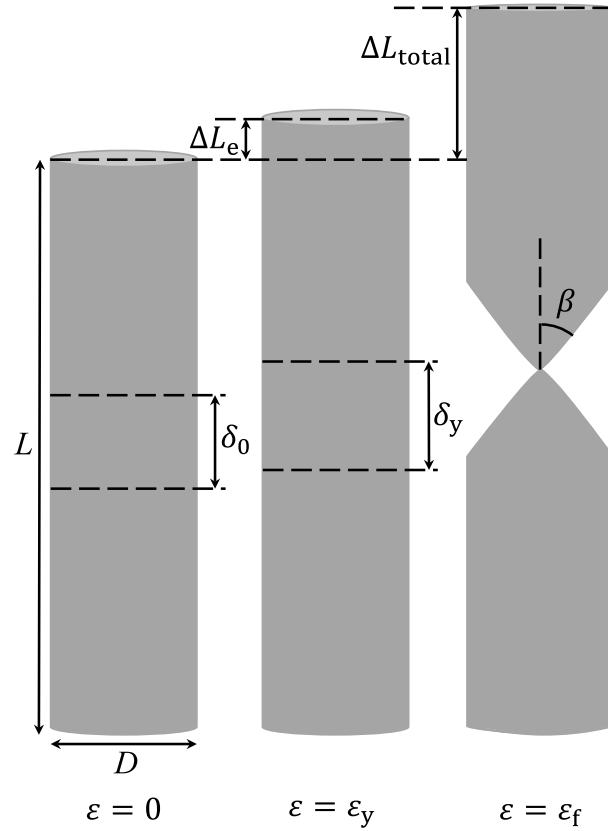
**Fig. 7.** Schematic illustration of fracture via necking. Nanowire has a cylindrical cross section. Only a nanowire with high aspect ratio deforms in necking mode under uniaxial tension.

### 4.4. Necking model

In analogy to the shear banding case, a fracture angle $\beta \approx 36°$ is noticed from MD simulations in the necking mode, as sketched in the cartoon shown in Fig. 7 and has been verified by the deformation pattern. Afterwards the effective strain in localization region can be expressed as follows

$$\varepsilon_{\text{eff}} = \frac{D}{\delta_0 \tan \beta} - \frac{\delta_y}{\delta_0} + \varepsilon_y. \tag{8}$$

One can establish a correlation between the fracture strain $\varepsilon_f$ and the aspect ratio in the necking mode by considering Eqs. (4) and (8), which reads

$$\varepsilon_f = \frac{D}{L \tan \beta} - \frac{\delta_y}{L} + \varepsilon_y. \tag{9}$$

Here, $\delta_y = (1 + \varepsilon_y)\delta_0$ and $\delta_0 = aL + bD$, therefore,

$$\varepsilon_f = \left( \frac{1}{\tan \beta} - a' \right) \frac{D}{L} - b' + \varepsilon_y, \tag{10}$$

in which the new parameters $a' = (1 + \varepsilon_y) a$ and $b' = (1 + \varepsilon_y) b$.

### 4.5. Validation of theoretical model

The two simple models capture the essential nature of size-dependent fracture modes in the amorphous nanowires, which can be validated by the MD simulations. To simplify the model, we have ignored the complex coupling between necking and shear banding. The fracture strains for $Cu_{50}Zr_{50}$ nanowires are summarized and displayed as a function of the reciprocal aspect ratio $D/L$ in Fig. 8, together with the theoretical predictions from shear banding (solid lines) and necking (dashed lines), respectively. The solid symbols indicate the wires fail in shear banding, while the open symbols correspond to the cases of necking fracture. It is seen that the MD date are in good agreement with the predicted $\varepsilon_f$ by either of the fracture model. Surprisingly, for all the $Cu_{50}Zr_{50}$ nanowires, $\varepsilon_f$
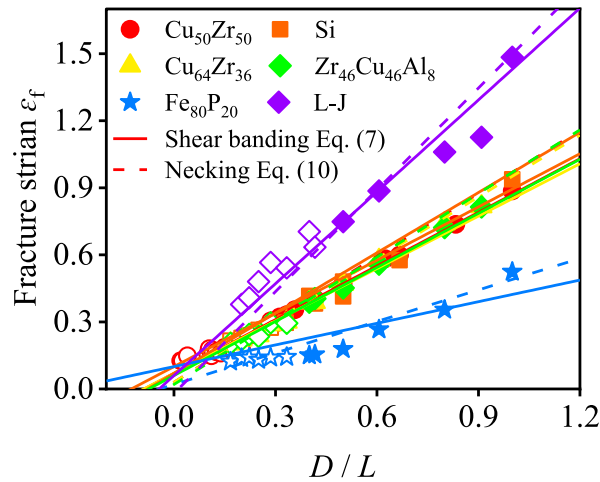
**Fig. 8.** Fracture strain vs $D/L$ for amorphous solids with different bonding nature, in which the ductile LJ system sets up an upper bound of ductility while the brittle FeP system supplies a lower bound of fracture strain. The solid lines represent prediction from shear banding model Eq. (7), and the dashed lines denote predictions from necking model Eq. (10).

grows with increasing $D/L$ with the same rate, regardless of the fracture mode. Therefore, the contribution of deformation mode to $\varepsilon_{\mathrm{f}}$ is trivial, while the aspect ratio is the governing factor in fracture.

### 4.6. Universality of scaling relationship in fracture

To demonstrate the universality of the scaling law between $\varepsilon_{\mathrm{f}}$ and $D/L$, the MD simulations are extended to other five amorphous materials including monatomic Si (Stillinger and Weber, 1985), binary $Cu_{64}Zr_{36}$ (Mendelev et al., 2009), $Fe_{80}P_{20}$ (Ackland et al., 2004), ternary $Zr_{46}Cu_{46}Al_8$ (Cheng et al., 2009), as well as the general L-J model (Kob and Andersen, 1995). These amorphous materials are representatives of different bonding natures, covering monatomic, binary, and ternary systems of both metallic and covalent bonding characteristics. Results about these MD simulations are further shown in Figs. A.2–A.11. The MD data and the model predictions for all the six amorphous materials are also summarized in Fig. 8. For different glasses, it is encouraging to see that the failure data of all nanowires overlap with theories. However, the fracture strains of the surveyed amorphous systems show different increasing rates with the aspect ratio. The most ductile L-J nanowires can bare more plastic strain while the most brittle one $Fe_{80}P_{20}$ nanowires are on the contrary. Therefore, the two systems set up upper and lower bound of ductility in the amorphous systems, defining a regime where the $Cu_{50}Zr_{50}$, Si, $Zr_{46}Cu_{46}Al_8$, and $Cu_{64}Zr_{36}$ wires reside and overlap with each other.

## 5. Discussion

### 5.1. Fracture normalized by elastic moduli

The fracture of materials has deep origin in the atomic interactions described by quantum mechanics. Here we provide such a bottom-up strategy for predicting fracture in nanoscale amorphous solids with input information down to the nature of chemical bonding. This is driven by the common sense that the brittle/ductile nature of a material is closely associated with the elastic properties, e.g., the Poisson's ratio $v$ and the ratio of shear modulus to bulk modulus $G/K$ (Wang, 2006; Lewandowski et al., 2005; Wang, 2012), as commonly used as empirical rules in the literature. A general trend is that the higher the Poisson's ratio (or the lower the $G/K$ ratio), the more ductile the material. A daily-life knowledge is that metals are more ductile than ceramics, the latter is of covalent bonding with very low Poisson's ratio. Therefore, $G/K$ and $v$ are also empirically used to judge the brittleness of MGs (Wang, 2012). This is consistent with the plots in Fig. 8, where L-J and $Fe_{80}P_{20}$ designed with the same aspect ratio but exhibit distinct elongation and, therefore, tensile ductility. More examples of moduli in other systems are further shown in Tables 1 and 2, where experimental data (from Tang et al., 2004; Madou, 2014; Xu et al., 2004; Wang, 2006; Chou et al., 1977; Gilabert et al., 2003) are available from calibration of simulations. Note that we adopt a Kob–Anderson two-body LJ potential that is different from the usual LJ. Therefore, the moduli of LJ metallic glasses from the two potentials differ significantly. To unify the observations, we have reduced all the simulated fracture strains by either $G/K$ or $1/v$, see Fig. 9a and b, respectively. It is found that all data collapse on a single line. Therefore, modulus normalized fracture strain is proportional to $D/L$. This trend does make sense since the phenomenon indicates that fracture behavior is not only governed by external factors, e.g., dimension and geometry, but also the intrinsic nature like chemical bonding, which indeed matters critically in fracture. In one words, it is the synergistic cooperation of intrinsic nature and extrinsic geometry that determines fracture in amorphous nanowires. Furthermore, we have attempted to construct super relationship by fitting fracture strains normalized by other forms of $G/K$ or $1/v$, such as power law. Interestingly, all the fracture strain reduced by $(G/K)^{1.5}$ or $(1/v)^{1.3}$ yields the best data collapse rather than the liner scaling albeit the physical reason remains unknown. We believe this issue deserves further investigation and will be analyzed in future works.

**Table 1**

Summary of bulk modulus $K$ (GPa), shear modulus $G$ (GPa), Poisson's ratio $\nu$, Young's modulus $E$ (GPa) and $G/K$ for various metallic glasses.

| Glasses | This work (MD) | | | | | Experiments[a] | | | | |
|---|---|---|---|---|---|---|---|---|---|---|
| | $K$ | $G$ | $\nu$ | $E$ | $G/K$ | $K$ | $G$ | $\nu$ | $E$ | $G/K$ |
| $Cu_{50}Zr_{50}$ | 107.74 | 25.61 | 0.382 | 69.82 | 0.238 | 101.20 | 31.30 | 0.360 | 85.03 | 0.309 |
| Si | 134.37 | 31.88 | 0.390 | 79.90 | 0.237 | 97.27 | 33.83 | 0.344 | 90.92 | 0.348 |
| $Cu_{64}Zr_{36}$ | 128.59 | 26.10 | 0.398 | 72.24 | 0.203 | 104.30 | 34.00 | 0.352 | 92.00 | 0.326 |
| $Zr_{46}Cu_{46}Al_8$ | 114.38 | 25.12 | 0.381 | 68.94 | 0.220 | 116.40 | 34.30 | 0.366 | 93.72 | 0.294 |
| $Fe_{80}P_{20}$ | 121.46 | 48.60 | 0.323 | 123.77 | 0.400 | 162.68 | 63.70 | 0.300 | 165.62 | 0.392 |

[a]These experimental data are from Tang et al. (2004), Madou (2014), Xu et al. (2004), Wang (2006), Chou et al. (1977).

**Table 2**

Summary of bulk modulus $K$, shear modulus $G$, Poisson's ratio $\nu$, Young's modulus $E$ and $G/K$ for LJ metallic glasses.

| Glass | This work (MD) | | | | | Reference[a] | | | | |
|---|---|---|---|---|---|---|---|---|---|---|
| | $K$ | $G$ | $\nu$ | $E$ | $G/K$ | $K$ | $G$ | $\nu$ | $E$ | $G/K$ |
| LJ | 81.12 | 13.79 | 0.409 | 60.37 | 0.170 | 52.49 | 13.70 | 0.380 | 37.85 | 0.261 |

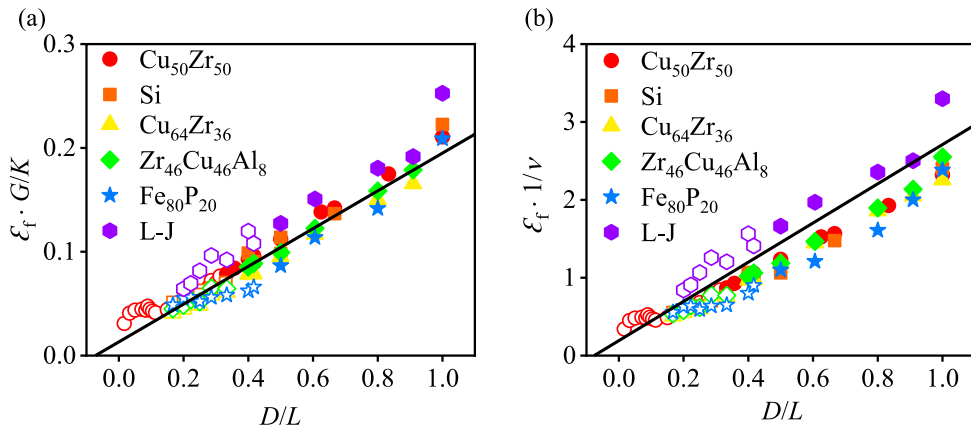[a]These MD simulations data are from Gilabert et al. (2003).



**Fig. 9.** Reduced fracture strain as a function of $D/L$ for several different amorphous solids, in which the fracture strain has been multiplied by $G/K$ in (a) and $1/\nu$ in (b), respectively. The solid symbols represent failure by shear banding while open symbols failure via necking. All data points collapse on a solid line that is proportional to $D/L$.

*5.2. Ideal strain from atomic interaction*

In addition, a critical step is to find an atomistically informed and physically sound parameter to correlate the fracture behaviors. This is essentially related to the interatomic interaction. As a consequence, we examine all the pair potential functions in Fig. 10. Although the details of potential curves varies according to different interaction, they share common trend. With increasing the atom–atom distance, all the pair functions behave in similar manner that potential energy decrease from infinite (strongest repulsive) to the stable state valley (energy minimum) and finally converge to zero potential energy (no interaction). Those functions capture the essence of the bond strength. Due to $\mathbf{F} = -\partial E(\mathbf{r})/\partial \mathbf{r}$, the force approaches to zero as potential energy goes to local minimum. As demonstrated further in Fig. 11, the stable position is $r_0$, where $\mathbf{F} = 0$. Then, a critical distance $r_c$ is defined when $\mathbf{F}$ reaches maximum value because the condition for fracture is satisfied at $r_c$ (uniform yielding). As a result, an atomic-scale ideal strain (upper bound strain of yielding) from stable state to instability can be calculated as

$$\varepsilon_{ideal} = \frac{r_c - r_0}{r_0}. \tag{11}$$

The ideal strain for binary and ternary systems are estimated from the weighted average scheme according to the concentration of each element. More details about the method can be found in Appendix. Table 3 summarizes the stable distance $r_0$, unstable distance $r_c$ and the ideal strain $\varepsilon_{ideal}$, respectively, for all the considered empirical potentials. As a matter of course, the lowest value of $\varepsilon_{ideal}$ corresponds to the most brittle glass $Fe_{80}P_{20}$. On the other hand, the highest $\varepsilon_{ideal}$ suggests the most ductile L-J glass. The findings are quite intriguing since it points to a direction that fracture has deep physical origin in atomic bonding.
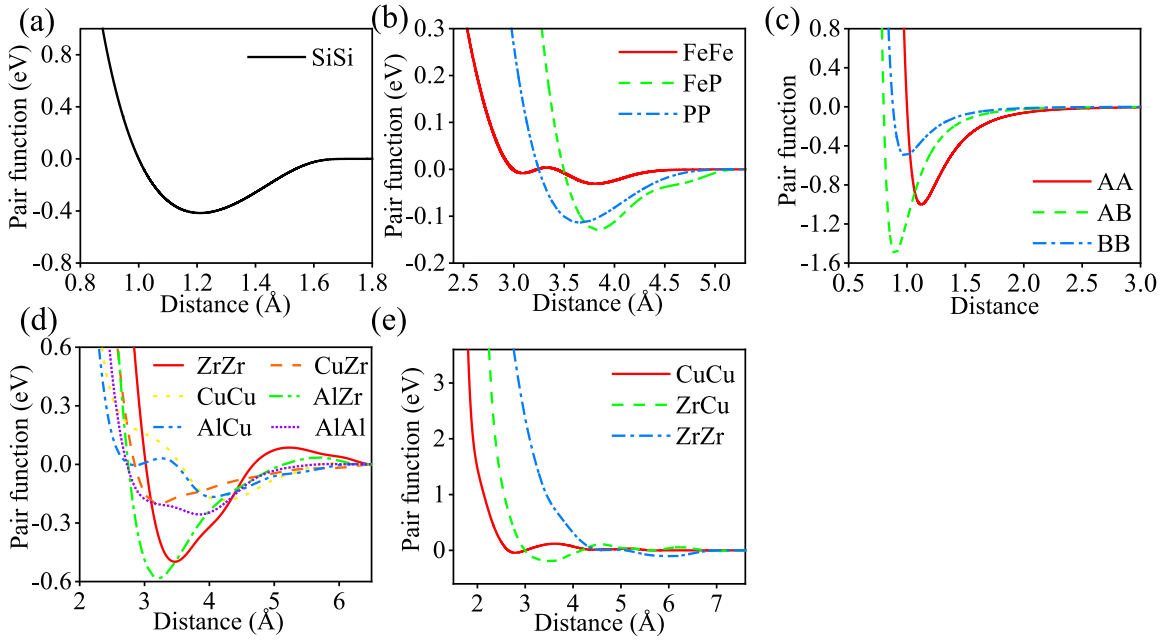
**Fig. 10.** Pair potentials calculated from (a) SW potential for Si, (b) EAM potential for FeP system, (c) Lennard-Jones potential, (d) EAM potential for ZrCuAl system, and (e) EAM potential for CuZr, respectively.
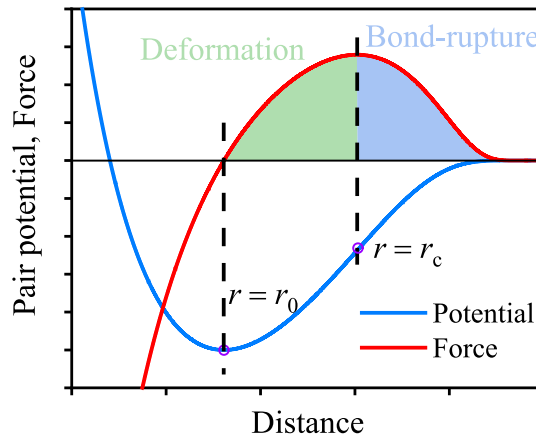


**Fig. 11.** Schematic illustration of the pair potential and force between two atoms. We choose the lowest position and the maximum positive derivative of the pair function as the parameters to idealize the fracture strain. The force between two atoms is equal to the negative derivative of the pair potential with respect to distance. The lowest point of potential means $\mathbf{F} = 0$, while another point indicates maximum force. At the same time, the two locations represent stable and unstable state between two atoms, respectively.

**Table 3**
The stable distance $r_0$, unstable distance $r_c$ and the corresponding ideal strain $\varepsilon_{ideal}$ defined from different empirical potentials for various glasses.

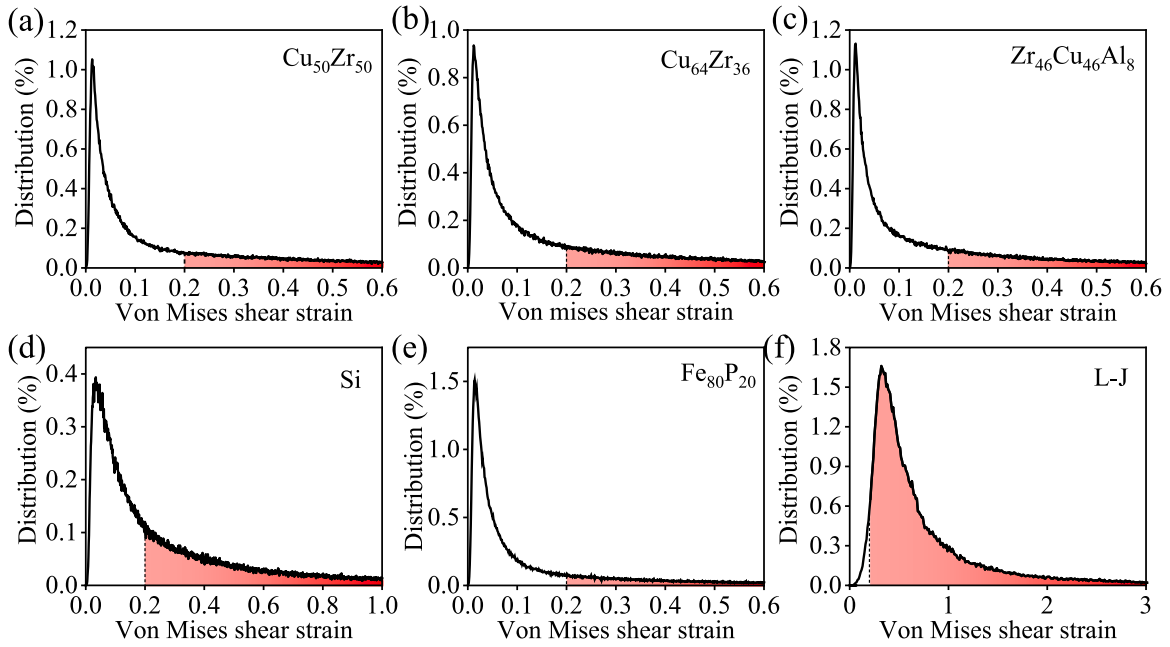| Glasses | A-A | | A-B | | B-B | | A-C | | B-C | | C-C | | $\varepsilon_{ideal}$ |
|---|---|---|---|---|---|---|---|---|---|---|---|---|---|
| | $r_0$ | $r_c$ | $r_0$ | $r_c$ | $r_0$ | $r_c$ | $r_0$ | $r_c$ | $r_0$ | $r_c$ | $r_0$ | $r_c$ | |
| $Cu_{50}Zr_{50}$ | 2.78 | 3.03 | 3.59 | 3.85 | 6.06 | 6.46 | | | | | | | 0.075 |
| Si | 1.22 | 1.34 | | | | | | | | | | | 0.099 |
| $Cu64Zr_{36}$ | 2.78 | 3.03 | 3.59 | 3.85 | 6.06 | 6.46 | | | | | | | 0.078 |
| $Zr_{46}Cu_{46}Al_8$ | 3.46 | 3.74 | 3.21 | 3.39 | 4.21 | 4.77 | 3.20 | 3.64 | 2.85 | 3.03 | 3.84 | 4.40 | 0.084 |
| $Fe_{80}P_{20}$ | 3.09 | 3.20 | 3.84 | 4.10 | 3.57 | 4.07 | | | | | | | 0.052 |
| L-J | 1.12 | 1.24 | 0.90 | 1.00 | 0.99 | 1.10 | | | | | | | 0.108 |

**Fig. 12.** Distributions of von Mises shear strain of six different systems near fracture. We define an atom that participates in plastic deformation with a strain greater than 0.2.

**Table 4**
Summary of participation atoms ratio $\chi$ near fracture for various glasses.

| Glasses | $Cu_{50}Zr_{50}$ | $Cu_{64}Zr_{36}$ | $Zr_{46}Cu_{46}Al_8$ | Si | $Fe_{80}P_{20}$ | LJ |
|---|---|---|---|---|---|---|
| Participation atoms ratio $\chi$ | 0.478 | 0.478 | 0.493 | 0.523 | 0.303 | 0.968 |

### 5.3. Participation ratio

Another important factor relevant to fracture of amorphous wires is that the fraction of the atoms participating in the localized deformation. To reveal the number, the atoms with atomic-scale von Mises shear strain invariant higher than 0.2 are deemed as the plastic ones. A further parameter $\chi$ is defined as the ratio of the plastic atoms to all atoms at the close-proximity of fracture. The distribution of von Mises shear strain in all the six different glassy systems near fracture are plotted in Fig. 12. The red shadow regions over the total area under the distribution curves represent the participation ratio $\chi$. Take a glance of the shadow area, it is deduded that the most ductile L-J system is of the highest $\chi$. However, there are very few plastic atoms in the brittle FeP system, in consistent with the limited fracture strain in FeP glass.

Furthermore, Fig. 13a demonstrates the spatial feature of the atomic shear strain in three typical glasses including $Fe_{80}P_{20}$, $Cu_{50}Zr_{50}$ and LJ. It confirms that $\chi$ is proportional to the ductility of these amorphous materials. The participation ratios are summarized in Table 4 for all the investigated glasses. Details about simulations of all systems are provided in Figs. A.14–A.17. In Fig. A.17, it is quite inspiring to see that participation ratio increases linearly with atomic ideal strain $\varepsilon_{ideal}$. Simultaneously, the fraction of expected deformation $\delta_0/L$ scales linearly with $\varepsilon_{ideal}$. All of them contribute to fracture and, therefore, tensile ductility of amorphous solids. It indicates that one should consider both ideal strain and participation ratio in understanding fracture.

### 5.4. Fracture universality

Once the participation ratio and atomic-scale ideal strain is available, one has an opportunity to translate the nominal fracture strain to an intrinsic physical property. This is done by normalizing the macroscopic fracture strain $\varepsilon_f$ by product of participation ratio and ideal strain, $\chi\varepsilon_{ideal}$, which yields a physical fracture strain $\varepsilon_f/(\chi\varepsilon_{ideal})$ that dictates the size effect of fracture. Fig. 13b illustrates the magnitudes of $\varepsilon_f/(\chi\varepsilon_{ideal})$ as a function of $D/L$. No matter what the amorphous system is, the size effect on nanowires can be depicted by a single master curve,

$$\varepsilon_f/(\chi\varepsilon_{ideal}) \sim D/L, \tag{12}$$

regardless of the fracture mode involved.

All the normalized fracture strain collapse on this single line, confirming the universality of the scaling law between fracture and aspect ratio. Note that the physical fracture strain has excluded the intrinsic properties of atomic bonding as well as participation ratio of plastic atoms, the scaling law reflect a pure size effect on fracture of amorphous solids. This operation represents a successful
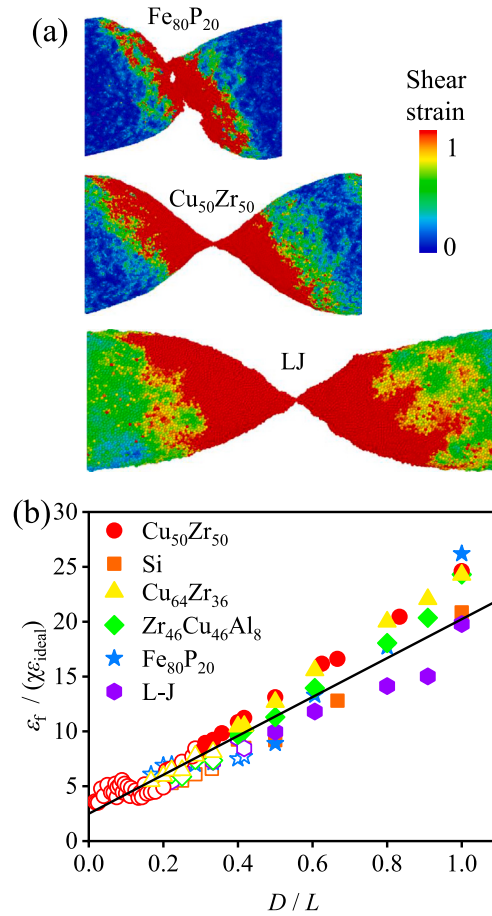
**Fig. 13.** Universal fracture law down to intrinsic nature of atomic bonding. (a) Failure modes of different amorphous systems (with dimensions $L = 20$ nm, and $D = 20$ nm) demonstrated by atomic shear strain at failure. (b) Data collapse on a scaling law $\varepsilon_f / (\chi \varepsilon_{ideal}) \sim D/L$ once the failure strain is normalized by the product of the participation ratio $\chi$ and an atomic ideal strain $\varepsilon_{ideal}$ defined by the interatomic potential. Solid symbols represent shear banding and open symbols necking.

demonstration of the bottom-up approach down to atomic scale to predict the macroscopic fracture behaviors of amorphous materials. Additionally, the data collapse also confirms the universality of the scaling law, which is also in accord with the theoretical predictions by Eqs. (7) and (10). In sum, the aspect ratio plays a pivotal role in fracture mode and ductility of nanoscale glasses once unfair participation ratio is excluded in the localized deformation.

## 6. Conclusion

In sum, extensive molecular dynamics simulations reveal a universal scaling law between fracture strain and aspect ratio of a wide variety of nanoscale amorphous glass wires. A fracture diagram of nanoscale glass is built after the simulations data which enables to recognize a critical aspect ratio $L : D \approx 3$ separating shear banding and necking as the dominating fracture mode. The observation was rationalized by two mechanistic models, assuming shear banding and necking as the size-dependent mechanisms, which interpret MD fracture results and enable theoretical prediction of fracture strains of various sized systems. By considering an intrinsic atomic-level yielding strain defined, we establish a robust relationship between the physical fracture strain – nominal fracture strain normalized by the product of atomic ideal strain and participation ratio of plastic atoms – and external geometry (i.e., aspect ratio) of nanowires. The fracture universality in different glasses indicate an intrinsic size effect in mechanics of amorphous materials regardless of the fracture mode. It should be noted that the fracture mechanism is closely related to the thermodynamic stability of the glassy configurations since they are energetically metastable materials. Atomistic samples are usually much rejuvenated states which is prone to experience ductile mode such as necking. However, the well-aged glass samples (e.g., those experimental samples) should be of more brittle nature. This trend has been witnessed recently by ultra-stable glasses which demonstrated very sharp shear banding fracture phenomenon (Su et al., 2022). It therefore highlights the physical origin of microscopic fracture in atomic-scale bonding nature of amorphous materials. The established scaling law suggests proper processing and fabrication strategies to control geometry of samples, which is a necessary prerequisite to prepare fracture-tolerant amorphous materials evading unexpected catastrophic failure.

**CRediT authorship contribution statement**

**Kun Zhao:** Methodology, Software, Visualization, Data curation, Writing – original draft. **Yun-Jiang Wang:** Conceptualization, Supervision, Writing – review & editing, Funding acquisition. **Penghui Cao:** Conceptualization, Supervision, Writing – review & editing.

**Declaration of competing interest**

The authors declare that they have no known competing financial interests or personal relationships that could have appeared to influence the work reported in this paper.

**Data availability**

Data will be made available on request.

**Acknowledgments**

**Appendix**

All of the atomic configurations in present work are visualized by the OVITO software (Stukowski, 2010) after calculations of displacement vector, atomic shear strain and non-affine squared displacement. To quantitatively measure the length of the strain localization region, we plot the spatial distribution of the averaged atomic shear strain along the tensile direction, As shown in Fig. A.1b. It is worth noting that the plastic-deformed atoms with high values of shear strain locate at regions of 34 nm < z < 57 nm, which is actually the position of the localized region. Then, the initial length of localized region is obtained via

$$\delta_0 = \frac{\delta_{\text{ob}} - (0.14 - \varepsilon_{\text{y}})L}{1 + \varepsilon_{\text{y}}}. \tag{A.1}$$
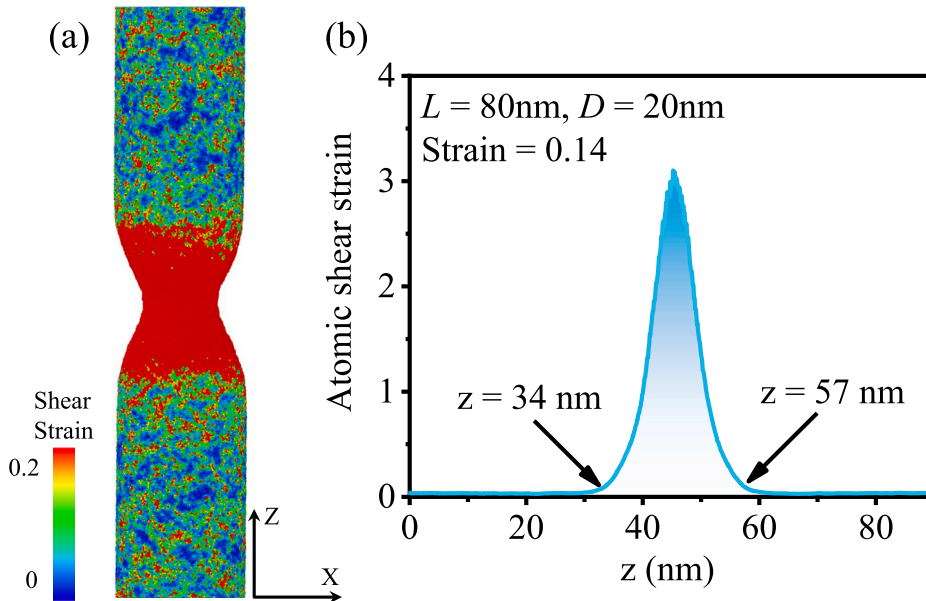


**Fig. A.1.** Observation and measurement of localized region for necking mode. (a) A snapshot at strain of 0.14 when localized region has already formed. Atoms are colored by the atomic shear strain. (b) Spatial distribution of atomic shear strain along direction of tension. Here 34 nm < z < 57 nm denotes the position of localized region.
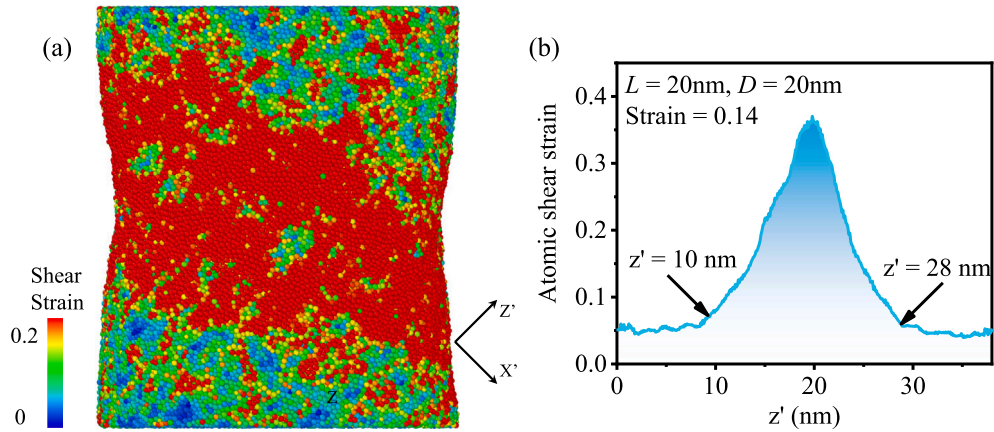
**Fig. A.2.** Observation and measurement of localized region for shear banding mode. (a) A snapshot at strain of 0.14 when shear band has already formed. Atoms are colored by the atomic shear strain. (b) Spatial distribution of atomic shear strain along direction perpendicular to shear band. Here 10 nm < z < 28 nm denotes the position of localized region.
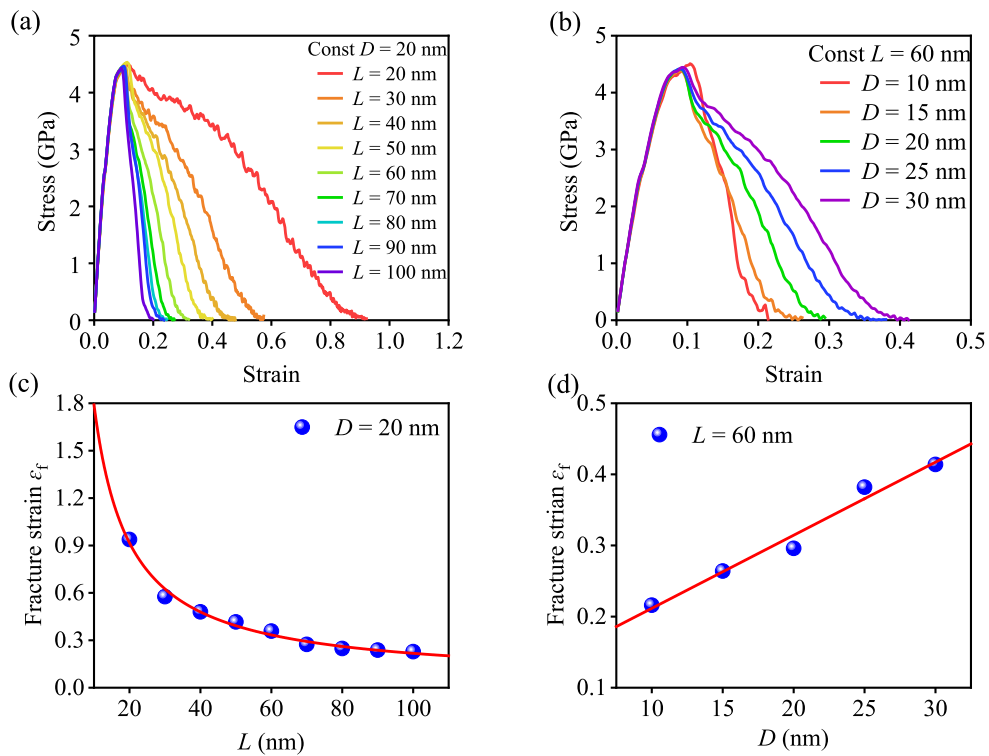


**Fig. A.3.** Diagram of deformation of amorphous silicon nanowires. (a) Stress–strain curves of nanowires with constant diameter 20 nm and varying length from 20 nm to 100 nm. (b) Stress–strain curves of nanowires with constant length 60 nm, but varying diameter from 10 to 30 nm. (c) Fracture strain decreases with increasing length. The solid curves represent best fit according to $\varepsilon_f \propto 1/L$. (d) Fracture strain increases linearly with diameter of nanowires.

**Table A.1**
Summary of the length of localization region $\delta_0$ and degree of localization $\delta_0/L$ near fracture for various glasses.

| Glasses | $Cu_{50}Zr_{50}$ | $Cu64Zr_{36}$ | $Zr_{46}Cu_{46}Al_8$ | Si | $Fe_{80}P_{20}$ | LJ |
|---|---|---|---|---|---|---|
| $\delta_0$(nm) | 12.4 | 12.8 | 12.6 | 13.2 | 8.8 | 17.2 |
| $\delta_0/L$ | 0.62 | 0.64 | 0.63 | 0.66 | 0.41 | 0.86 |
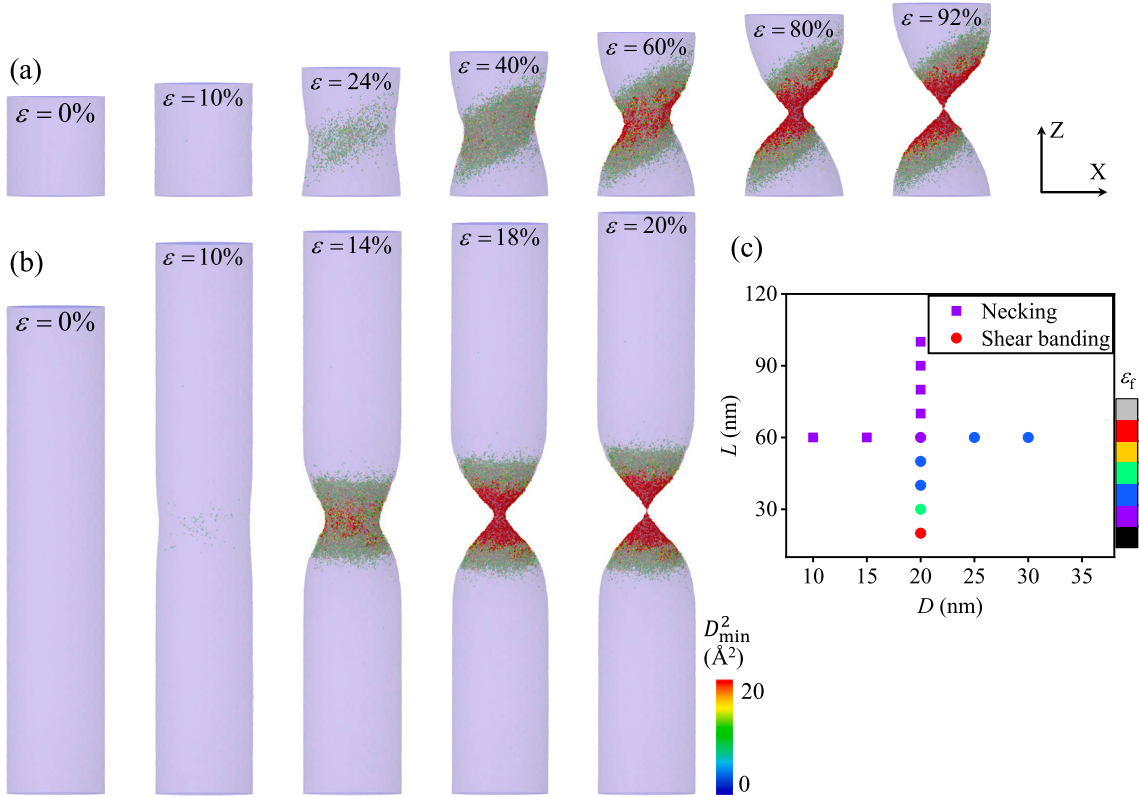


**Fig. A.4.** The size-dependent deformation mechanism of amorphous silicon nanowires. Snapshots of the behavior of (a) shear banding in fat wire ($L = 20$ nm, $D = 20$ nm) and (b) necking in thin wire ($L = 100$ nm, $D = 20$ nm) colored by non-affine squared displacement at different strain states. Only atoms with displacement more than 10 Å were reserved for clear observation. (c) Deformation-mechanism map of nanowires indicated by the magnitude of the fracture strain $\varepsilon_f$. Square symbols indicate necking mode, and circular symbols indicate shear banding mode.

Similarly, the measurement of $\delta_0$ for shear banding mode is shown in Fig. A.2. But the atomic strain coarse-graining orientation is perpendicular to the direction of the shear band instead of the macroscopic tensile direction in necking. Upon calculation of $\delta_0$, the strain localization length should be projected back to the direction of tension.

Next, we collect all $\delta_0$ of $Cu_{50}Zr_{50}$ metallic glass nanowires and study the relationship between $\delta_0$ and the sample size. We find that for nanowires with the same diameter, $\delta_0$ is proportional to the length of samples. Similarly, $\delta_0$ increases with the growth of the diameter of samples. Finally, the function of $\delta_0$ with respect to sample size is written as

$$\delta_0 = aL + bD. \tag{A.2}$$

The following figures from Figs. A.3 to A.12 are the MD simulations of five other amorphous systems, including Si (Stillinger and Weber, 1985), $Cu_{64}Zr_{36}$ (Mendelev et al., 2009), $Zr_{46}Cu_{46}Al_8$ (Cheng et al., 2009), $Fe_{80}P_{20}$ (Ackland et al., 2004), as well as the general Lennard-Jones (LJ) model (Kob and Andersen, 1995). Generally, all data are reflecting the same phenomenon. Size effect on nanowires fracture can be summarized as: (I) fracture strain $\varepsilon_f$ is proportional to diameter and is inversely proportional to length; (II) fracture strain $\varepsilon_f$ is directly influenced by the aspect ratio of nanowires; (III) nanowires with low aspect ratio deform in shear banding mode, while the high-aspect-ratio nanowires fail in necking mode. No matter which amorphous system nanowires is, they behave in the same manner under uniaxial tension. However it is rather remarkable that the brittle $Fe_{80}P_{20}$ metallic glass nanowires bear the least plastic strain due to massive cavitation behaviors during tension. But the ductile L-J metallic glass nanowires bear the most plastic deformation because they retain more liquid property after quenching.
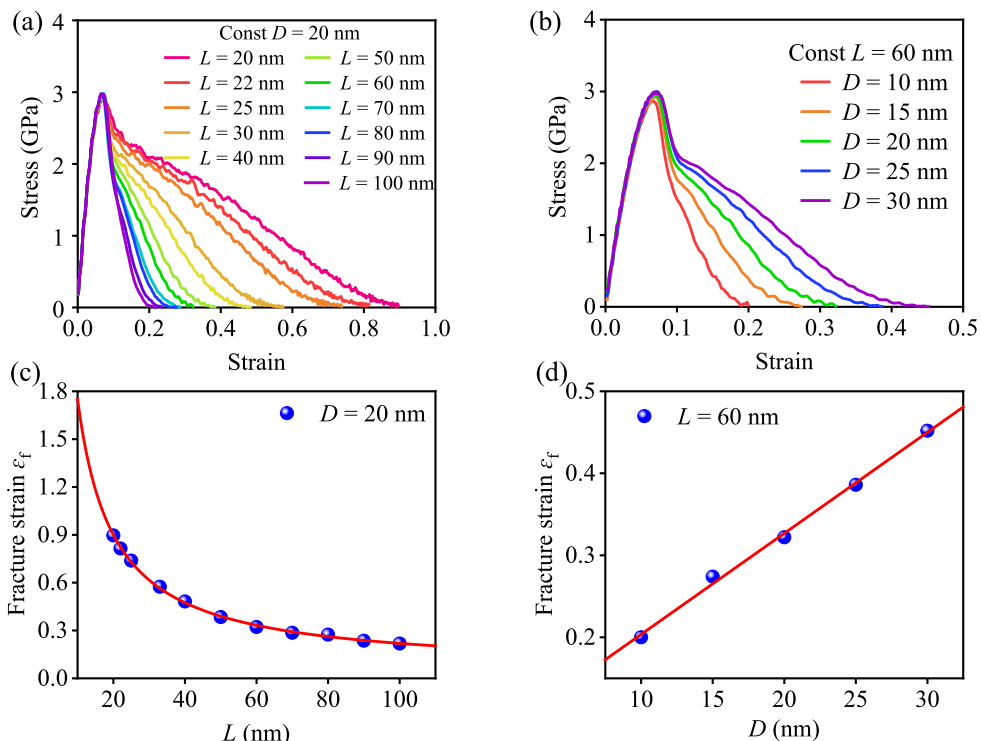
**Fig. A.5.** Diagram of deformation of $Cu_{64}Zr_{36}$ metallic glass nanowires. (a) Stress–strain curves of nanowires with constant diameter 20 nm and varying length from 20 nm to 100 nm. (b) Stress–strain curves of nanowires with constant length 60 nm, but varying diameter from 10 to 30 nm. (c) Fracture strain decreases with increasing length. The solid curves represent best fit according to $\varepsilon_f \propto 1/L$. (d) Fracture strain increases linearly with diameter of nanowires.
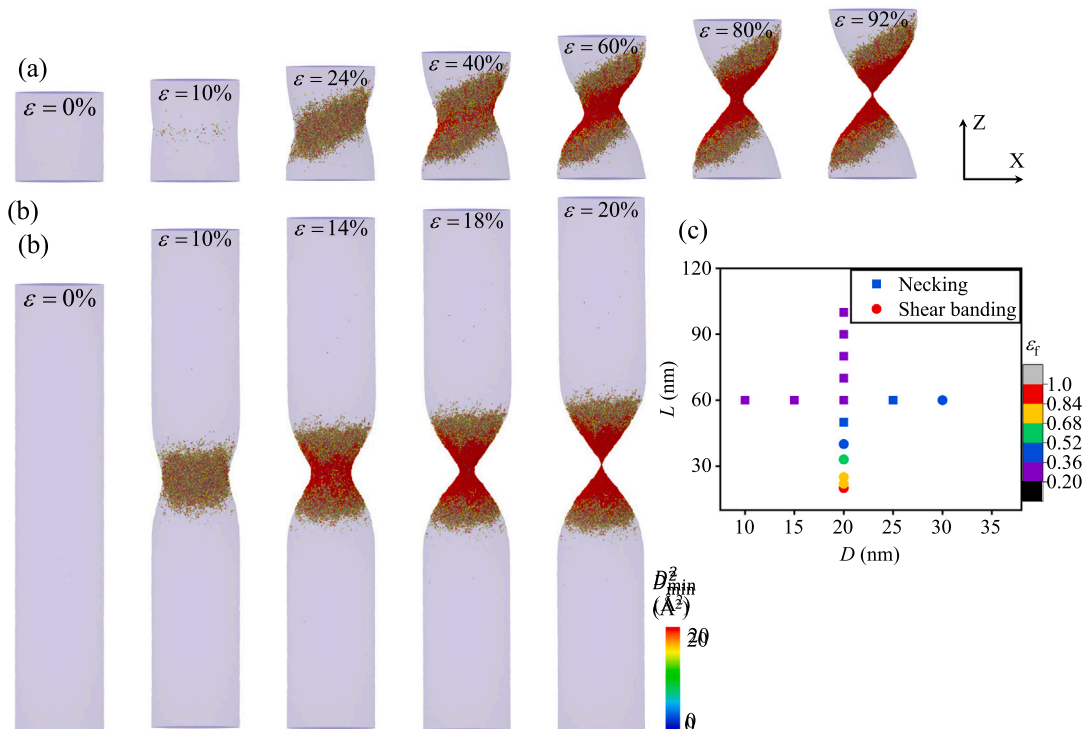


**Fig. A.6.** The size-dependent deformation mechanism of $Cu_{64}Zr_{36}$ metallic glass nanowires. Snapshots of the behavior of (a) shear banding in fat wire ($L = 20\,\text{nm}, D = 20\,\text{nm}$) and (b) necking in thin wire ($L = 100\,\text{nm}, D = 20\,\text{nm}$) colored by non-affine squared displacement at different strain states. Only atoms with displacement more than 12 Å were reserved for clear observation. (c) Deformation-mechanism map of nanowires indicated by the magnitude of the fracture strain $\varepsilon_f$. Square symbols indicate necking mode, and circular symbols indicate shear banding mode.
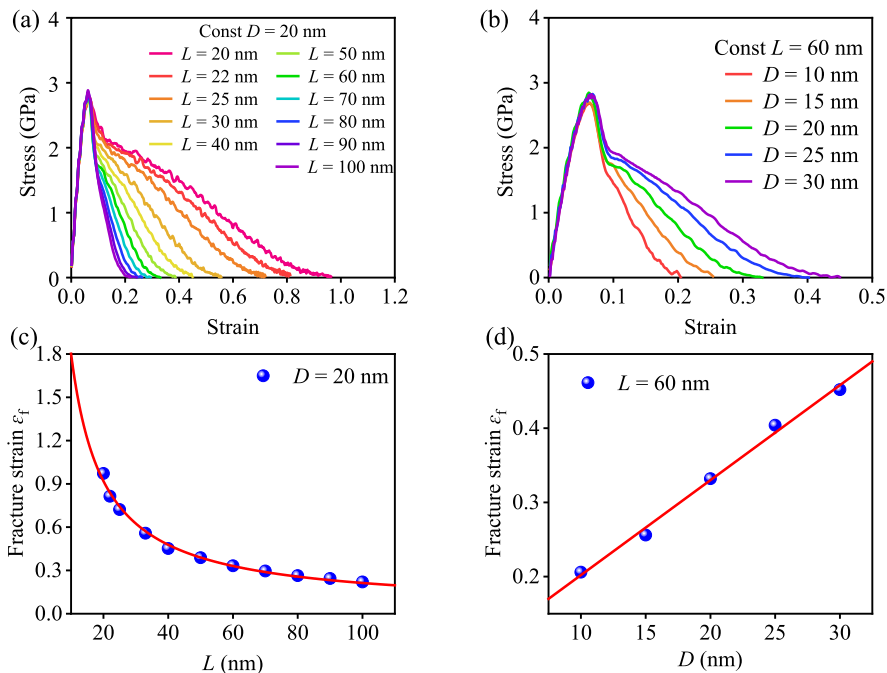
**Fig. A.7.** Diagram of deformation of $Zr_{46}Cu_{46}Al_8$ metallic glass nanowires. (a) Stress–strain curves of nanowires with constant diameter 20 nm and varying length from 20 nm to 100 nm. (b) Stress–strain curves of nanowires with constant length 60 nm, but varying diameter from 10 to 30 nm. (c) Fracture strain decreases with increasing length. The solid curves represent best fit according to $\varepsilon_f \propto 1/L$. (d) Fracture strain increases linearly with diameter of nanowires.
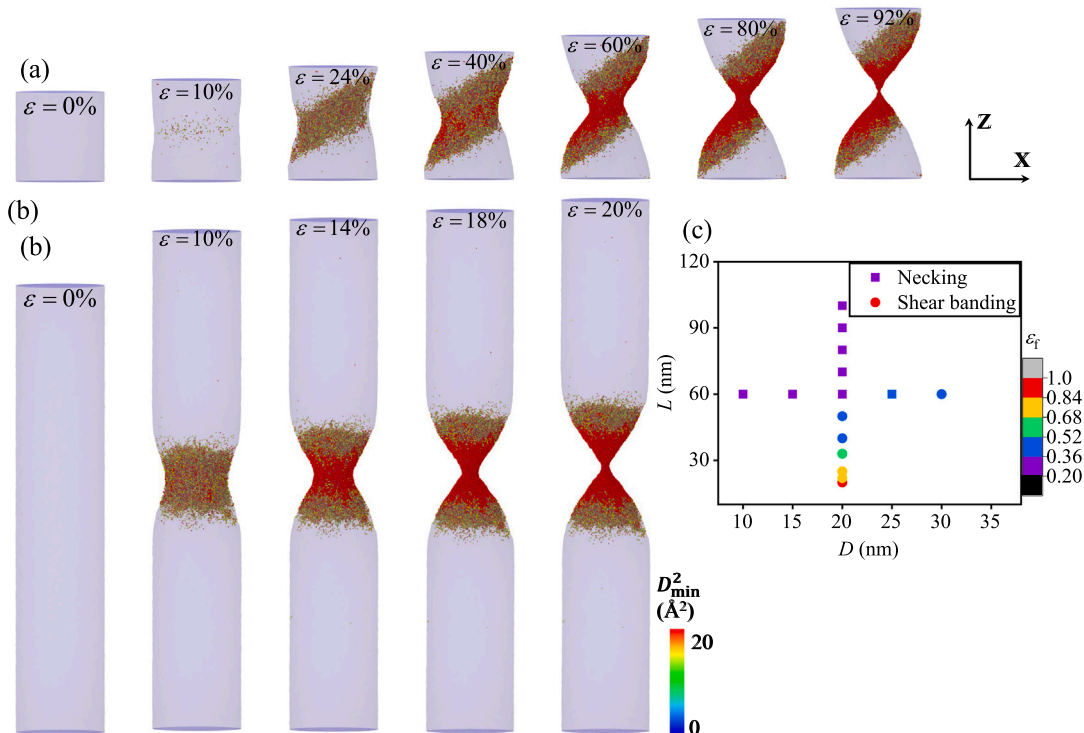


**Fig. A.8.** The size-dependent deformation mechanism of $Zr_{46}Cu_{46}Al_8$ metallic glass nanowires. Snapshots of the behavior of (a) shear banding in fat wire ($L = 20\,\text{nm}, D = 20\,\text{nm}$) and (b) necking in thin wire ($L = 100\,\text{nm}, D = 20\,\text{nm}$) colored by non-affine squared displacement at different strain states. Only atoms with displacement more than 13 Å were reserved for clear observation. (c) Deformation-mechanism map of nanowires indicated by the magnitude of the fracture strain $\varepsilon_f$. Square symbols indicate necking mode, and circular symbols indicate shear banding mode.

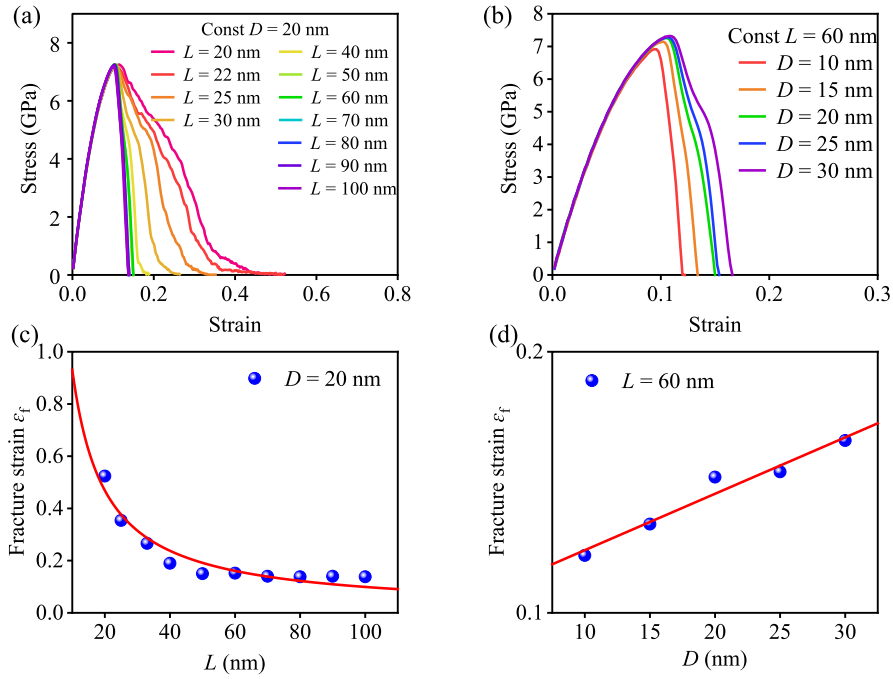**Fig. A.9.** Diagram of deformation of $Fe_{80}P_{20}$ metallic glass nanowires. (a) Stress–strain curves of nanowires with constant diameter 20 nm and varying length from 20 nm to 100 nm. (b) Stress–strain curves of nanowires with constant length 60 nm, but varying diameter from 10 to 30 nm. (c) Fracture strain decreases with increasing length. The solid curves represent best fit according to $\varepsilon_f \propto 1/L$. (d) Fracture strain increases linearly with diameter of nanowires.

Further studies on those two amorphous systems are shown in Figs. A.13 and A.14. The displacement fields in the two systems are generally identical and in compliance with that in $Cu_{50}Zr_{50}$ metallic glass nanowires. At the same time, we find a lot of cavitation defects in the displacement field in $Fe_{80}P_{20}$ metallic glass nanowires which well forcasts the brittle nature of $Fe_{80}P_{20}$.

We also examine the nature of several pair potential functions containing amorphous Si (Stillinger and Weber, 1985), $Cu_{64}Zr_{36}$ metallic glass (Mendelev et al., 2009), $Zr_{46}Cu_{46}Al_8$ metallic glass (Cheng et al., 2009), $Fe_{80}P_{20}$ metallic glass (Ackland et al., 2004), as well as the general LJ model (Kob and Andersen, 1995), in determining ideal atomic strain. In general, all functions are in the same trend. Therefore, we choose two significant atomic distance as the key characteristic of fracture as shown in Fig. 11 in the main text. First of all, $\mathbf{F} = \partial E/\partial \mathbf{r}$. Thus, at the blue point, i.e. $r_0$ in Fig. 11,

$$\mathbf{F} = -\frac{\partial E}{\partial \mathbf{r}} = 0. \tag{A.3}$$

And at the red point, i.e. $r_c$ in Fig. 11,

$$\begin{cases} \mathbf{F} = -\frac{\partial E}{\partial \mathbf{r}} \quad \text{reach} \quad \text{maximum,} \\ \frac{\partial^2 E}{\partial^2 \mathbf{r}} = 0. \end{cases}$$

Thus, the ideal strain $\varepsilon_{ideal}$ can be defined as:

$$\varepsilon_{ideal} = \frac{r_c - r_0}{r_0}. \tag{A.4}$$

Additionally, for monatomic system, we can directly calculate the ideal strain utilizing Eq. (A.4). Yet we need to get a weighted average of ideal strain for binary and ternary systems. The method is simple, for binary systems $A_xB_{(1-x)}$:

$$\varepsilon_{ideal} = x[x\varepsilon_{idealAA} + (1-x)\varepsilon_{idealAB}] + (1-x)[x\varepsilon_{idealAB} + (1-x)\varepsilon_{idealBB}]. \tag{A.5}$$

For ternary systems $A_xB_yC_{(1-x-y)}$:

$$\begin{aligned} \varepsilon_{ideal} = {} & x[x\varepsilon_{idealAA} + y\varepsilon_{idealAB} + (1-x-y)\varepsilon_{idealAC}] \\ & + y[x\varepsilon_{idealBA} + y\varepsilon_{idealBB} + (1-x-y)\varepsilon_{idealBC}] \\ & + (1-x-y)[x\varepsilon_{idealCA} + y\varepsilon_{idealCB} + (1-x-y)\varepsilon_{idealCC}]. \end{aligned} \tag{A.6}$$
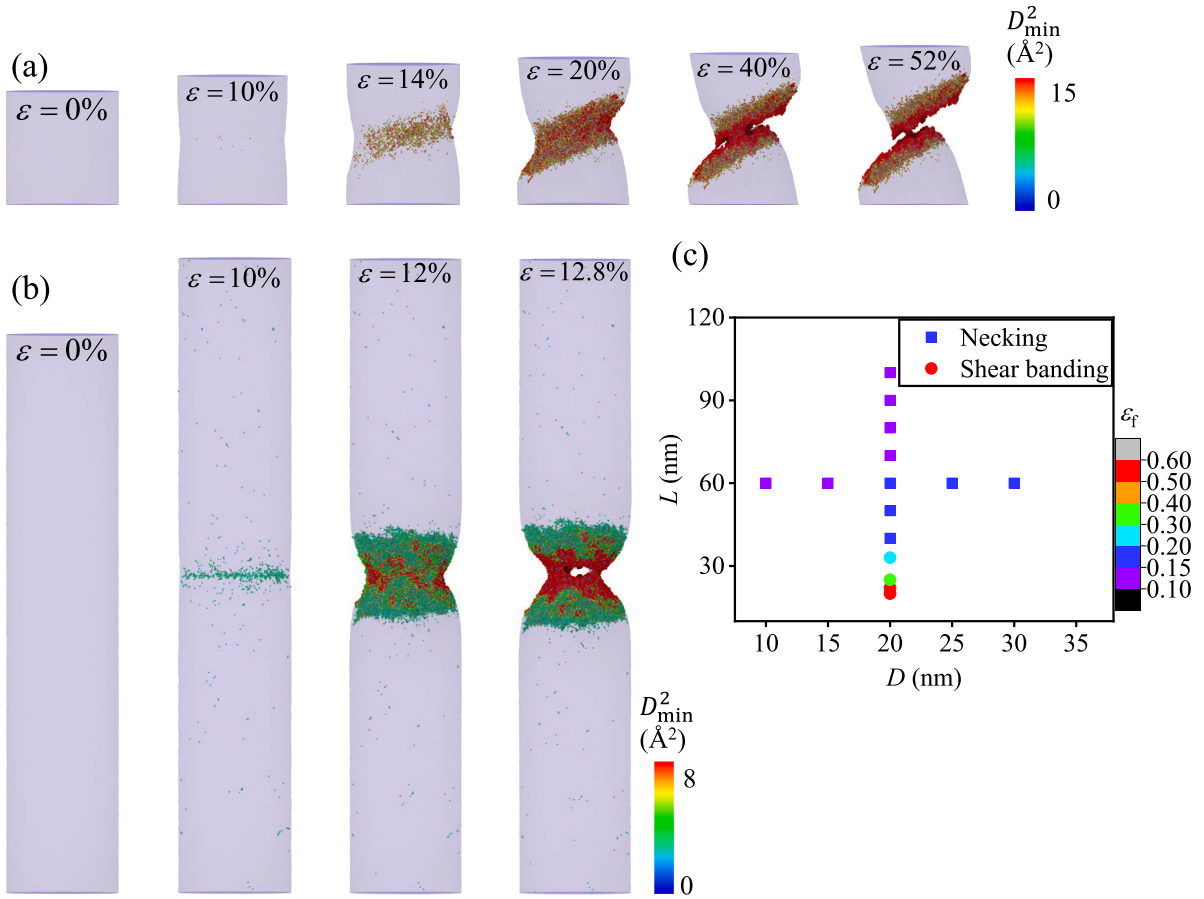
**Fig. A.10.** The size-dependent deformation mechanism of $Fe_{80}P_{20}$ metallic glass nanowires. Snapshots of the behavior of (a) shear banding in fat wire ($L = 20$ nm, $D = 20$ nm) and (b) necking in thin wire ($L = 100$ nm, $D = 20$ nm) colored by non-affine squared displacement at different strain states. Only atoms with displacement more than 10 Å were reserved for clear observation. (c) Deformation-mechanism map of nanowires indicated by the magnitude of the fracture strain $\varepsilon_f$. Square symbols indicate necking mode, and circular symbols indicate shear banding mode.

Finally, we collect all data of six different amorphous systems in Table 3 in the main text. As a matter of course, the lowest $\varepsilon_{ideal}$ corresponds to the most brittle glass $Fe_{80}P_{20}$ and the highest $\varepsilon_{ideal}$ belongs to the most ductile L-J glass.

We choose six nanowires with the same initial size but different systems and observe the atomic shear strain near fracture by OVITO. The snapshots are shown in Fig. A.15. The distributions of those shear strain are drew in Fig. 11. Theoretically the atoms with an atomic scale strain greater than 0.2 can be considered as the active participants of plastic deformation. So the red shadow in Fig. 11 represent the participation atoms ratio $\chi$. Summary of those data is shown in Table 4.

Interestingly, we find $\chi$ is proportional to the ductility of amorphous systems. As illustrated in Fig. A.16, participation ratio of deformed atoms $\chi$ is linear with the atomic ideal strain $\varepsilon_{ideal}$.

From another point of view, we can achieve the involvement of plastic deformation of nanowires by computing the length of localization region that contains all plastic atoms. Thus, Fig. A.17 shows the localization region of six different nanowires in terms of coloring the atoms with the same color coding range. We get the length $\delta_0$ and the ratio $\delta_0/L$ which indicates the degree of localization. Akin to the relationship between $\chi$ and $\varepsilon_{ideal}$, the fraction of expected deformation $\delta_0/L$ is proportional to $\varepsilon_{ideal}$ as shown in Fig. A.18. Therefore, it is believed that the more ductile nanowires are, the more plastic atoms there are. And the relevant data are summarized in Table A.1.
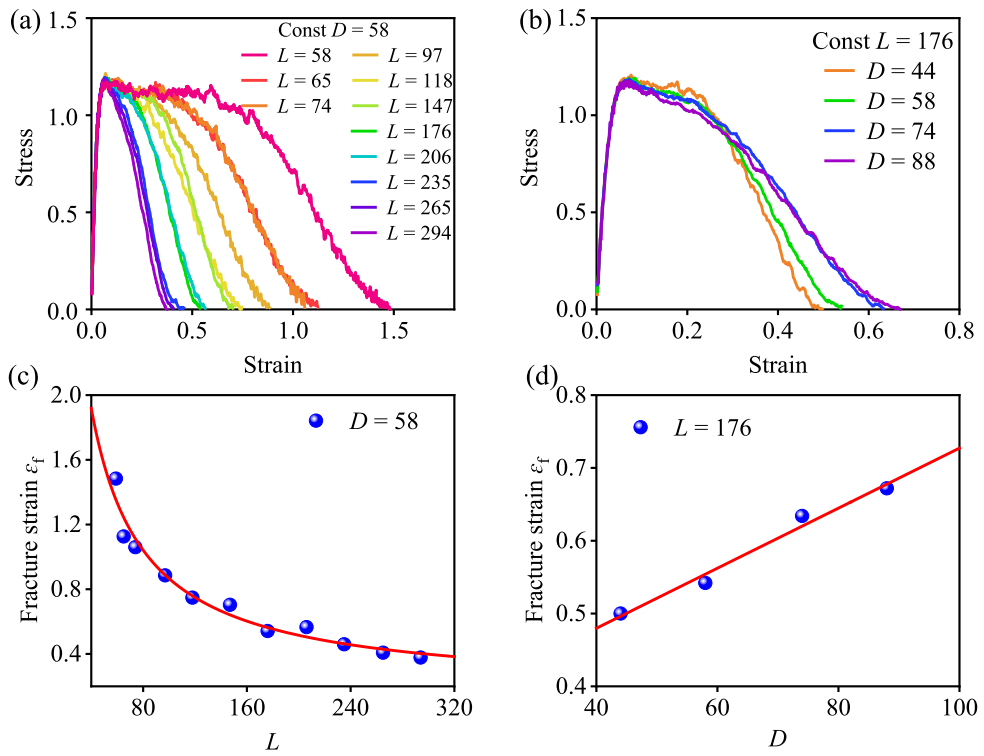
**Fig. A.11.** Diagram of deformation of LJ metallic glass nanowires. (a) Stress–strain curves of nanowires with constant diameter 58 and varying length from 58 to 294. (b) Stress–strain curves of nanowires with constant length 176, but varying diameter from 44 to 88. (c) Fracture strain decreases with increasing length. The solid curves represent best fit according to $\varepsilon_f \propto 1/L$. (d) Fracture strain increases linearly with diameter of nanowires.
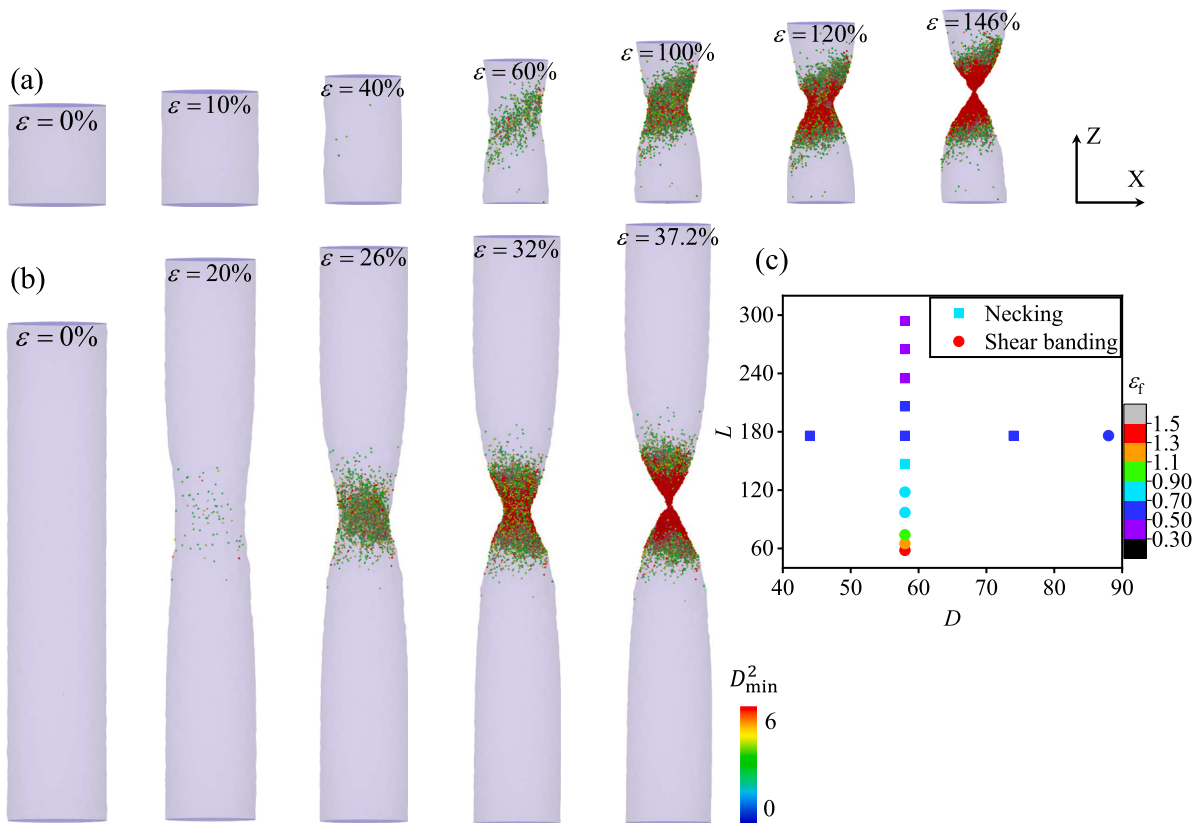
**Fig. A.12.** The size-dependent deformation mechanism of LJ metallic glass nanowires. Snapshots of the behavior of (a) shear banding in fat wire ($L = 58$, $D = 58$) and (b) necking in thin wire ($L = 294$, $D = 58$) colored by non-affine squared displacement at different strain states. Only atoms with displacement more than 3 were reserved for clear observation. (c) Deformation-mechanism map of nanowires indicated by the magnitude of the fracture strain $\varepsilon_f$. Square symbols indicate necking mode, and circular symbols indicate shear banding mode.
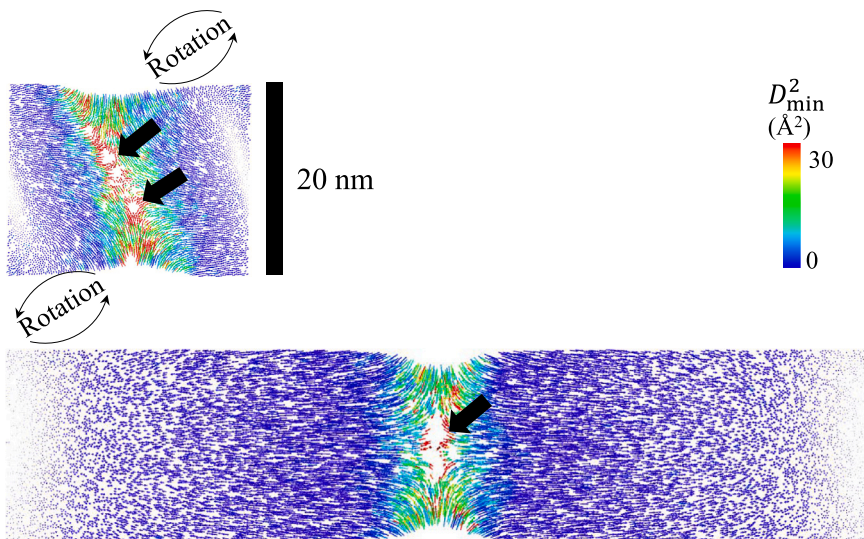


**Fig. A.13.** This displacement field in $Fe_{80}P_{20}$ metallic glass nanowires with small aspect ratio 1:1 and large aspect ratio 4:1. Two nanowires are under tensile strain $\varepsilon = 0.24$ and $\varepsilon = 0.12$, respectively. For clarity, the displacement vector has been scaled by 0.5.
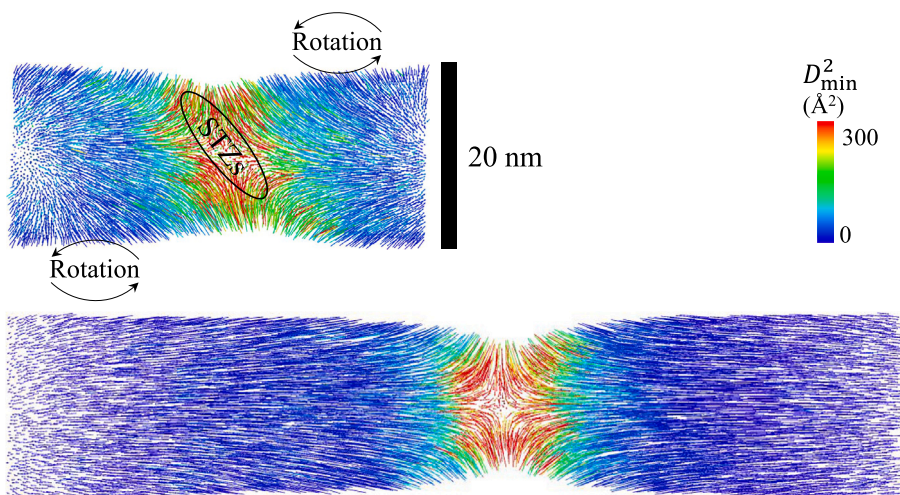
**Fig. A.14.** This displacement field in LJ metallic glass nanowires with small aspect ratio 1:1 and large aspect ratio 4:1. Two nanowires are under tensile strain $\varepsilon = 1$ and $\varepsilon = 0.36$, respectively. For clarity, the displacement vector has been scaled by 0.5.
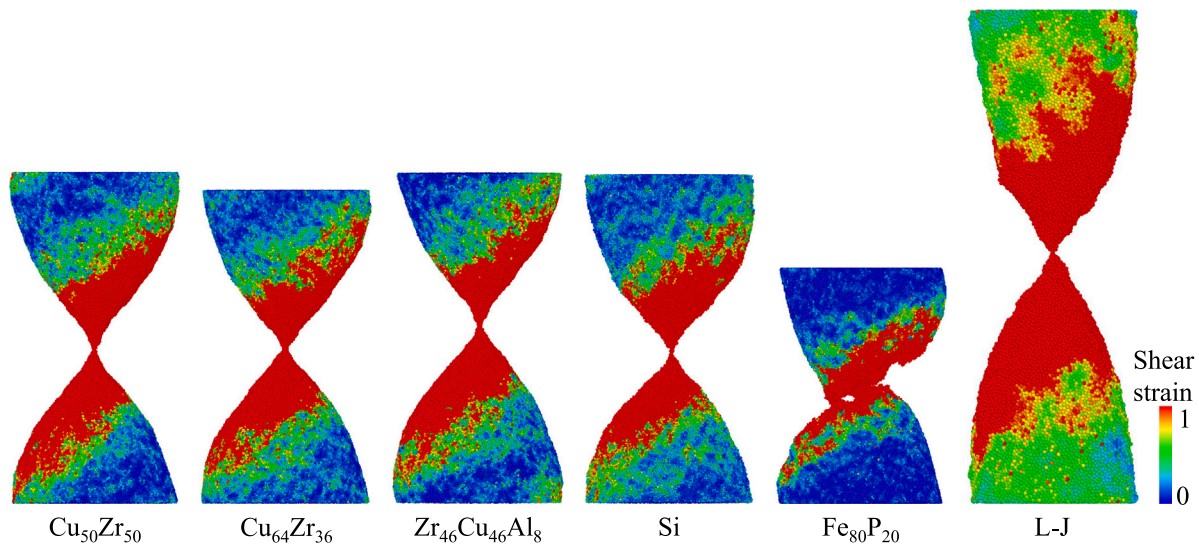


**Fig. A.15.** Snapshots of the behavior of six nanowires with the same initial size ($L = 20$ nm, $D = 20$ nm) but different amorphous systems. Atoms are colored by shear strain with same color coding range.
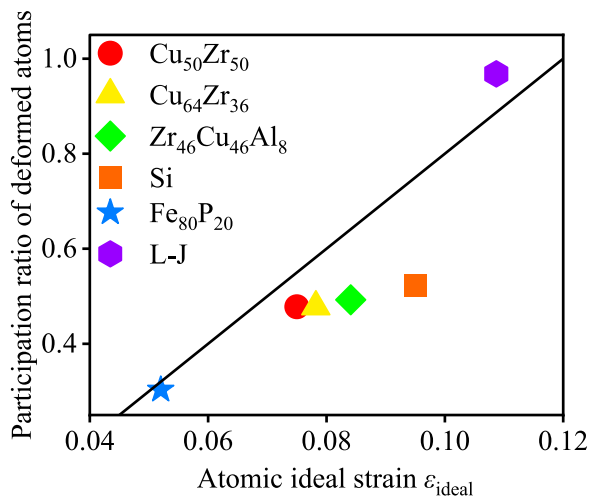
**Fig. A.16.** Relationship between participation atoms ratio with atomic ideal strain $\varepsilon_{\text{ideal}}$.
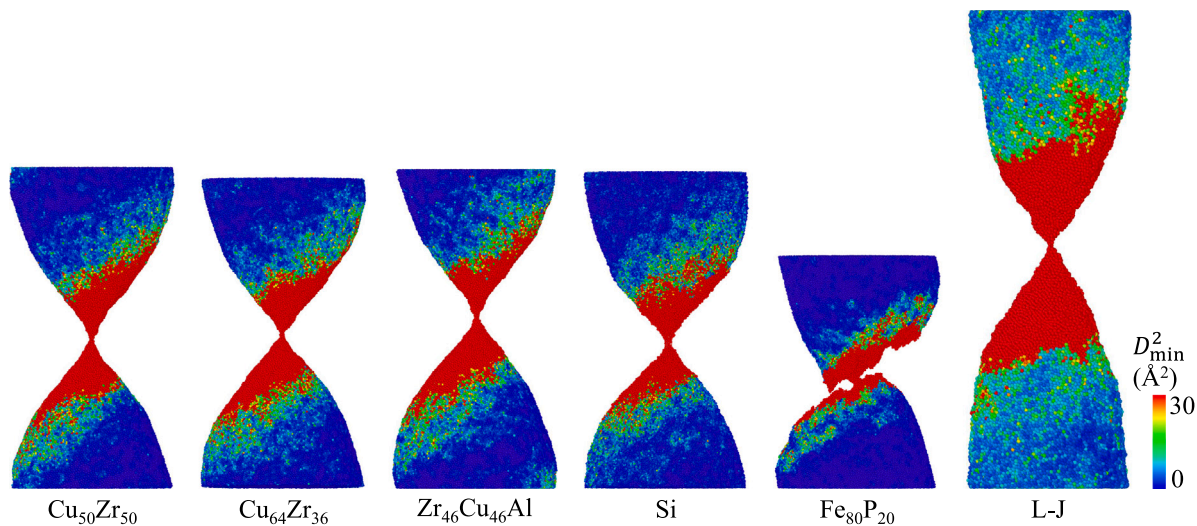


**Fig. A.17.** Snapshots of the behavior of six nanowires with the same initial size ($L = 20$ nm, $D = 20$ nm) but different amorphous systems. We can observe the strain localized zone near fracture and derive $\delta_0$ from that. Finally, we got degree of localization $\delta_0/L$ with different systems. Atoms are colored by non-affine squared displacement with the same color coding range.
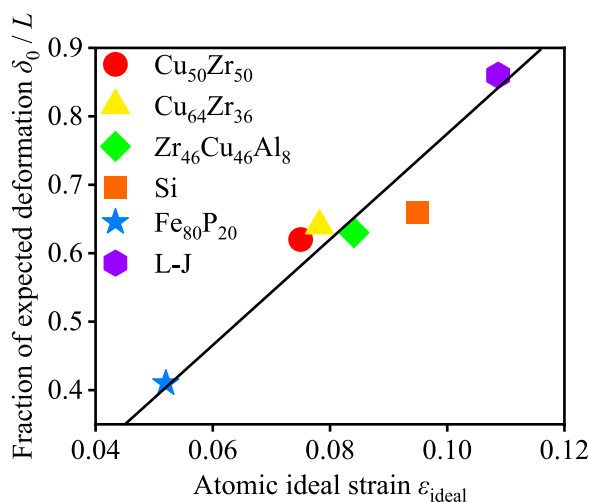
**Fig. A.18.** Relationship between degree of localization $\delta_0/L$ with atomic ideal strain $\varepsilon_{ideal}$.

# References

Ackland, G.J., Mendelev, M.I., Srolovitz, D.J., Han, S., Barashev, A.V., 2004. Development of an interatomic potential for phosphorus impurities in -iron. J. Phys.: Condens. Matter 16 (27), S2629–S2642. http://dx.doi.org/10.1088/0953-8984/16/27/003, arXiv:0406356.

Argon, A.S., 1979. Plastic deformation in metallic glasses. Acta Metall. 27 (1), 47–58. http://dx.doi.org/10.1016/0001-6160(79)90055-5.

Ashby, M.F., Greer, A.L., 2006. Metallic glasses as structural materials. Scr. Mater. 54 (3), 321–326. http://dx.doi.org/10.1016/j.scriptamat.2005.09.051.

Bonfanti, S., Ferrero, E.E., Sellerio, A.L., Guerra, R., Zapperi, S., 2018. Damage accumulation in silica glass nanofibers. Nano Lett. 18 (7), 4100–4106. http://dx.doi.org/10.1021/acs.nanolett.8b00469.

Cao, P., Dahmen, K.A., Kushima, A., Wright, W.J., Park, H.S., Short, M.P., Yip, S., 2018. Nanomechanics of slip avalanches in amorphous plasticity. J. Mech. Phys. Solids 114, 158–171.

Cao, P., Short, M.P., Yip, S., 2019. Potential energy landscape activations governing plastic flows in glass rheology. Proc. Natl. Acad. Sci. 116 (38), 18790–18797.

Chen, D.Z., Jang, D., Guan, K.M., An, Q., Goddard, W.A., Greer, J.R., 2013. Nanometallic glasses: Size reduction brings ductility, surface state drives its extent. Nano Lett. 13 (9), 4462–4468. http://dx.doi.org/10.1021/nl402384r.

Cheng, Y.Q., Ma, E., Sheng, H.W., 2009. Atomic level structure in multicomponent bulk metallic glass. Phys. Rev. Lett. 102 (24), 245501. http://dx.doi.org/10.1103/PhysRevLett.102.245501.

Chou, C.-P., Davis, L., Narasimhan, M., 1977. Elastic constants of metallic glasses. Scr. Metall. 11 (5), 417–423. http://dx.doi.org/10.1016/0036-9748(77)90280-0, URL: https://doi.org/10.1016/0036-9748(77)90280-0https://linkinghub.elsevier.com/retrieve/pii/0036974877902800.

Christensen, R., Li, Z., Gao, H., 2018. An evaluation of the failure modes transition and the Christensen ductile/brittle failure theory using molecular dynamics. Proc. R. Soc. A Math. Phys. Eng. Sci. 474 (2219), http://dx.doi.org/10.1098/rspa.2018.0361.

Falk, M.L., Langer, J.S., 1998. Dynamics of viscoplastic deformation in amorphous solids. Phys. Rev. E 57 (6), 7192–7205. http://dx.doi.org/10.1103/PhysRevE.57.7192.

Gilabert, F., Krivtsov, A., Castellanos, A., 2003. Computer simulation of mechanical properties for powder particles using Molecular Dynamics. Proc XXX Summer Sch. (April 2014), 230–239.

Gludovatz, B., Naleway, S.E., Ritchie, R.O., Kruzic, J.J., 2014. Size-dependent fracture toughness of bulk metallic glasses. Acta Mater. 70, 198–207. http://dx.doi.org/10.1016/j.actamat.2014.01.062.

Greer, J.R., De Hosson, J.T.M., 2011. Plasticity in small-sized metallic systems: Intrinsic versus extrinsic size effect. Prog. Mater. Sci. 56 (6), 654–724. http://dx.doi.org/10.1016/j.pmatsci.2011.01.005.

Greer, A.L., Ma, E., 2007. Bulk metallic glasses: At the cutting edge of metals research. MRS Bull. 32 (8), 611–619. http://dx.doi.org/10.1557/mrs2007.121.

Griffith, A.A., 1921. VI. The phenomena of rupture and flow in solids. Philos. Trans. R. Soc. Lond. Ser. A Math. Phys. Eng. Sci. 221 (582–593), 163–198. http://dx.doi.org/10.1098/rsta.1921.0006.

Gu, X.W., Jafary-Zadeh, M., Chen, D.Z., Wu, Z., Zhang, Y.W., Srolovitz, D.J., Greer, J.R., 2014. Mechanisms of failure in nanoscale metallic glass. Nano Lett. 14 (10), 5858–5864. http://dx.doi.org/10.1021/nl5027869.

Guan, P., Lu, S., Spector, M.J.B., Valavala, P.K., Falk, M.L., 2013. Cavitation in amorphous solids. Phys. Rev. Lett. 110, 185502. http://dx.doi.org/10.1103/PhysRevLett.110.185502.

Guo, H., Yan, P.F., Wang, Y.B., Tan, J., Zhang, Z.F., Sui, M.L., Ma, E., 2007. Tensile ductility and necking of metallic glass. Nature Mater. 6 (10), 735–739. http://dx.doi.org/10.1038/nmat1984.

Hoover, W.G., 1985. Canonical dynamics: Equilibrium phase-space distributions. Phys. Rev. A 31 (3), 1695–1697. http://dx.doi.org/10.1103/PhysRevA.31.1695.

Jang, D., Greer, J.R., 2010. Transition from a strong-yet-brittle to astronger-and-ductile state by size reduction of metallic glasses. Nature Mater. 9 (3), 215–219. http://dx.doi.org/10.1038/nmat2622.

Klement, W., Willens, R.H., Duwez, P., 1960. Non-crystalline structure in solidified gold–silicon alloys. Nature 187 (4740), 869–870. http://dx.doi.org/10.1038/187869b0.

Kob, W., Andersen, H.C., 1995. Testing mode-coupling theory for a supercooled binary Lennard-Jones mixture I: The van Hove correlation function. Phys. Rev. E 51 (5), 4626–4641. http://dx.doi.org/10.1103/PhysRevE.51.4626.

Kumar, G., Desai, A., Schroers, J., 2011. Bulk metallic glass: The smaller the better. Adv. Mater. 23 (4), 461–476. http://dx.doi.org/10.1002/adma.201002148.

Lewandowski, J.J., Wang, W.H., Greer, A.L., 2005. Intrinsic plasticity or brittleness of metallic glasses. Phil. Mag. Lett. 85 (2), 77–87. http://dx.doi.org/10.1080/09500830500080474.

Li, F.C., Wang, S., He, Q.F., Zhang, H., Sun, B.A., Lu, Y., Yang, Y., 2017. The stochastic transition from size dependent to size independent yield strength in metallic glasses. J. Mech. Phys. Solids 109, 200–216. http://dx.doi.org/10.1016/j.jmps.2017.09.001.

Lu, L., Chen, X., Huang, X., Lu, K., 2009. Revealing the maximum strength in nanotwinned copper. Science 323 (5914), 607–610. http://dx.doi.org/10.1126/science.1167641.

Luo, J., Wang, J., Bitzek, E., Huang, J.Y., Zheng, H., Tong, L., Yang, Q., Li, J., Mao, S.X., 2016. Size-dependent brittle-to-ductile transition in silica glass nanofibers. Nano Lett. 16 (1), 105–113. http://dx.doi.org/10.1021/acs.nanolett.5b03070.

Madou, M.J., 2014. Fundamentals of macrofabrication. In: Dairy Sci. Technol. CRC Taylor Fr. Gr. (June), pp. 1–542.

Mendelev, M.I., Kramer, M.J., Ott, R.T., Sordelet, D.J., Yagodin, D., Popel, P., 2009. Development of suitable interatomic potentials for simulation of liquid and amorphous Cu-Zr alloys. Phil. Mag. 89 (11), 967–987. http://dx.doi.org/10.1080/14786430902832773.

Murali, P., Guo, T., Zhang, Y., Narasimhan, R., Li, Y., Gao, H., 2011. Atomic scale fluctuations govern brittle fracture and cavitation behavior in metallic glasses. Phys. Rev. Lett. 107, 215501. http://dx.doi.org/10.1103/PhysRevLett.107.215501.

Nosé, S., 1984. A molecular dynamics method for simulations in the canonical ensemble. Mol. Phys. 52 (2), 255–268. http://dx.doi.org/10.1080/00268978400101201.

Pan, J., Ivanov, Y.P., Zhou, W.H., Li, Y., Greer, A.L., 2020. Strain-hardening and suppression of shear-banding in rejuvenated bulk metallic glass. Nature 578 (7796), 559–562. http://dx.doi.org/10.1038/s41586-020-2016-3, https://doi.org/10.1038/s41586-020-2016-3.

Pan, J., Zhou, H.F., Wang, Z.T., Li, Y., Gao, H.J., 2015. Origin of anomalous inverse notch effect in bulk metallic glasses. J. Mech. Phys. Solids 84, 85–94. http://dx.doi.org/10.1016/j.jmps.2015.07.006, https://doi.org/10.1016/j.jmps.2015.07.006.

Parrinello, M., Rahman, A., 1981. Polymorphic transitions in single crystals: A new molecular dynamics method. J. Appl. Phys. 52, 7182. http://dx.doi.org/10.1063/1.328693, https://doi.org/10.1063/1.328693.

Plimpton, S., 1995. Fast parallel algorithms for short-range molecular dynamics. J. Comput. Phys. 117 (1), 1–19. http://dx.doi.org/10.1006/jcph.1995.1039.

Qu, R., Tönnies, D., Tian, L., Liu, Z., Zhang, Z., Volkert, C.A., 2019. Size-dependent failure of the strongest bulk metallic glass. Acta Mater. 178, 249–262. http://dx.doi.org/10.1016/j.actamat.2019.08.010.

Sha, Z.D., He, L.C., Xu, S., Pei, Q.X., Liu, Z.S., Zhang, Y.W., Wang, T.J., 2014. Effect of aspect ratio on the mechanical properties of metallic glasses. Scr. Mater. 93, 36–39. http://dx.doi.org/10.1016/j.scriptamat.2014.08.025.

Sha, Z., Wong, W.H., Pei, Q., Branicio, P.S., Liu, Z., Wang, T., Guo, T., Gao, H., 2017. Atomistic origin of size effects in fatigue behavior of metallic glasses. J. Mech. Phys. Solids 104, 84–95. http://dx.doi.org/10.1016/j.jmps.2017.04.005.

Shen, L.-Q., Yu, J.-H., Tang, X.-C., Sun, B.-A., Liu, Y.-H., Bai, H.-Y., Wang, W.-H., 2021. Observation of cavitation governing fracture in glasses. Sci. Adv. 7, abf7293. http://dx.doi.org/10.1126/sciadv.abf7293.

Shimizu, F., Ogata, S., Li, J., 2007. Theory of shear banding in metallic glasses and molecular dynamics calculations. Mater. Trans. 48 (11), 2923–2927. http://dx.doi.org/10.2320/matertrans.MJ200769.

Şopu, D., Foroughi, A., Stoica, M., Eckert, J., 2016. Brittle-to-ductile transition in metallic glass nanowires. Nano Lett. 16 (7), 4467–4471. http://dx.doi.org/10.1021/acs.nanolett.6b01636.

Şopu, D., Stukowski, A., Stoica, M., Scudino, S., 2017. Atomic-level processes of shear band nucleation in metallic glasses. Phys. Rev. Lett. 119, 195503. http://dx.doi.org/10.1103/PhysRevLett.119.195503.

Stillinger, F.H., Weber, T.A., 1985. Computer simulation of local order in condensed phases of silicon. Phys. Rev. B 31 (8), 5262–5271. http://dx.doi.org/10.1103/PhysRevB.31.5262.

Stukowski, A., 2010. Visualization and analysis of atomistic simulation data with OVITO–the Open Visualization Tool. Modelling Simul. Mater. Sci. Eng. 18 (1), 015012. http://dx.doi.org/10.1088/0965-0393/18/1/015012.

Su, R., Zhang, S., Zhang, X., Yang, Y., Wang, W., Guan, P., 2022. Atomic origin of annealing embrittlement in metallic glasses. pp. 1–38. http://dx.doi.org/10.48550/arXiv.2208.13747, arXiv:2208.13747.

Sun, B.A., Wang, W.H., 2015. The fracture of bulk metallic glasses. Prog. Mater. Sci. 74, 211–307. http://dx.doi.org/10.1016/j.pmatsci.2015.05.002.

Swallen, S.F., Kearns, K.L., Mapes, M.K., Kim, Y.S., McMahon, R.J., Ediger, M.D., Wu, T., Yu, L., Satija, S., 2007. Organic glasses with exceptional thermodynamic and kinetic stability. Science 315 (5810), 353–356. http://dx.doi.org/10.1126/science.1135795.

Taloni, A., Vodret, M., Costantini, G., Zapperi, S., 2018. Size effects on the fracture of microscale and nanoscale materials. Nat. Rev. Mater. 3 (7), 211–224. http://dx.doi.org/10.1038/s41578-018-0029-4.

Tang, M., Zhao, D., Pan, M., Wang, W., 2004. Binary Cu-Zr bulk metallic glasses. Chin. Phys. Lett. 21.

Tao, W., Cao, P., Park, H.S., 2018. Atomistic simulation of the rate-dependent ductile-to-brittle failure transition in bicrystalline metal nanowires. Nano Lett. 18 (2), 1296–1304.

Tian, L., Cheng, Y.-Q., Shan, Z.-W., Li, J., Wang, C.-C., Han, X.-D., Sun, J., Ma, E., 2012. Approaching the ideal elastic limit of metallic glasses. Nature Commun. 3, 609. http://dx.doi.org/10.1038/ncomms1619.

Tian, L., Shan, Z.W., Ma, E., 2013. Ductile necking behavior of nanoscale metallic glasses under uniaxial tension at room temperature. Acta Mater. 61 (13), 4823–4830. http://dx.doi.org/10.1016/j.actamat.2013.05.001.

Wang, W.H., 2006. Correlations between elastic moduli and properties in bulk metallic glasses. J. Appl. Phys. 99 (9), 093506. http://dx.doi.org/10.1063/1.2193060.

Wang, W.H., 2012. The elastic properties, elastic models and elastic perspectives of metallic glasses. Prog. Mater. Sci. 57 (3), 487–656. http://dx.doi.org/10.1016/j.pmatsci.2011.07.001.

Wang, C.-C., Ding, J., Cheng, Y.-Q., Wan, J.-C., Tian, L., Sun, J., Shan, Z.-W., Li, J., Ma, E., 2012. Sample size matters for Al88Fe7Gd5 metallic glass: Smaller is stronger. Acta Mater. 60 (13–14), 5370–5379. http://dx.doi.org/10.1016/j.actamat.2012.06.019.

Wang, H., Dmowski, W., Tong, Y., Wang, Z., Yokoyama, Y., Ketkaew, J., Schroers, J., Egami, T., 2022. Nonaffine strains control ductility of metallic glasses. Phys. Rev. Lett. 128 (15), 155501. http://dx.doi.org/10.1103/PhysRevLett.128.155501, https://doi.org/10.1103/PhysRevLett.128.155501.

Wei, Y., Bower, A.F., Gao, H., 2010. Analytical model and molecular dynamics simulations of the size dependence of flow stress in amorphous intermetallic nanowires at temperatures near the glass transition. Phys. Rev. B 81 (12), 125402. http://dx.doi.org/10.1103/PhysRevB.81.125402.

Wu, Z., Zhang, Y.W., Jhon, M.H., Gao, H., Srolovitz, D.J., 2012. Nanowire failure: Long = brittle and short = 'ductile. Nano Lett. 12 (2), 910–914. http://dx.doi.org/10.1021/nl203980u.

Wu, F.F., Zhang, Z.F., Mao, S.X., 2009. Size-dependent shear fracture and global tensile plasticity of metallic glasses. Acta Mater. 57 (1), 257–266. http://dx.doi.org/10.1016/j.actamat.2008.09.012.

Xu, D., Lohwongwatana, B., Duan, G., Johnson, W.L., Garland, C., 2004. Bulk metallic glass formation in binary Cu-rich alloy series - Cu 100-xZrx (x=34 , 36, 38.2, 40 at.%) and mechanical properties of bulk Cu64Zr36 glass. Acta Mater. 52 (9), 2621–2624. http://dx.doi.org/10.1016/j.actamat.2004.02.009.

Yang, Z.Y., Dai, L.H., 2021. Giant configurational softening controls atomic-level process of shear banding in metallic glasses. Phys. Rev. Mater. 5 (12), 1–8. http://dx.doi.org/10.1103/PhysRevMaterials.5.123602.

Yang, Q., Pei, C.-Q., Yu, H.-B., Feng, T., 2021a. Metallic nanoglasses with promoted $\beta$-relaxation and tensile plasticity. Nano Lett. 21 (14), 6051–6056. http://dx.doi.org/10.1021/acs.nanolett.1c01283.

Yang, Y., Zhou, J., Zhu, F., Yuan, Y., Chang, D.J., Kim, D.S., Pham, M., Rana, A., Tian, X., Yao, Y., Osher, S.J., Schmid, A.K., Hu, L., Ercius, P., Miao, J., 2021b. Determining the three-dimensional atomic structure of an amorphous solid. Nature 592 (7852), 60–64. http://dx.doi.org/10.1038/s41586-021-03354-0, arXiv:2004.02266.

Yu, H.B., Shen, X., Wang, Z., Gu, L., Wang, W.H., Bai, H.Y., 2012. Tensile plasticity in metallic glasses with pronounced $\beta$ relaxations. Phys. Rev. Lett. 108 (1), 015504. http://dx.doi.org/10.1103/PhysRevLett.108.015504.

Yu, H.B., Wang, W.H., Samwer, K., 2013. The $\beta$ relaxation in metallic glasses: an overview. Mater. Today 16 (5), 183–191. http://dx.doi.org/10.1016/j.mattod.2013.05.002.

Zhang, Y., Cao, P., Deng, B., Huang, L., Shi, Y., 2021. Strain rate-dependent tensile response of glassy silicon nanowires studied by accelerated atomistic simulations. J. Appl. Phys. 130 (8), 085105. http://dx.doi.org/10.1063/5.0060136.

Zhou, X., Zhou, H., Li, X., Chen, C., 2015. Size effects on tensile and compressive strengths in metallic glass nanowires. J. Mech. Phys. Solids 84, 130–144. http://dx.doi.org/10.1016/j.jmps.2015.07.018.